Aerodynamics of wind turbines

Horikiri, Kana

Aerodynamics of wind turbines

By:

Kana Horikiri

A thesis submitted for the degree of Master of Philosophy

to the University of London

January 2011

Supervised by:

Professor Theodosios Korakianitis

(a.k.a. Theodosios Alexander)

Dr Eldad Avital

Abstract

The study of rotor blade aerodynamic performances of wind turbine has been presented in this thesis. This study was focused on aerodynamic effects changed by blade surface distribution as well as grid solution along the airfoil. The details of numerical calculation from Fluent were described to help predict accurate blade performance for comparison and discussion with available data.

The direct surface curvature distribution blade design method for two-dimensional airfoil sections for wind turbine rotors have been discussed with the attentions to Euler equation, velocity diagram and the factors which affect wind turbine performance and applied to design a blade geometry close to an existing wind turbine blade, Eppler387, in order to argue that the blade surface drawn by direct surface curvature distribution blade design method contributes aerodynamic efficiency.

The FLUENT calculation of NACA63-215V showed that the aerodynamic characteristics agreed well with the available experimental data at lower angles of attack although it was discontinuities in the surface curvature distributions between 0.7 and 0.8 in x/c. The discontinuities were so small that the blade performance could not be affected.

The design of Eppler 387 blade performed to reduce drag force. The discontinuities of surface distribution matched the curve of the pressure coefficients. It was found in the curvature distribution that the leading edge pressure side had difficulties to connect to Bezier curve and also the trailing edge circle was never be tangent to the lines of trailing edge pressure and suction sides due to programming difficulties.

Contents

List of Tables

List of Figures

1 Introduction

1.1 Background

The reason why wind energy is concerned is when environmental issues such as climate change, acid rain and imbalance of natural resources have been developed all over the world by using a great number of coal, oil and gas as fuel in power generation. The primary fuels occupy about 90% of energy demand last two decades in the UK [1] as shown in Figure 1. Energy demand is increased by the rise in population. When people request to improve their lifestyle and material, it leads to accelerate the use of such energy. Hence it is important to create new energy and keep it as long in the appropriate level of emission as possible.

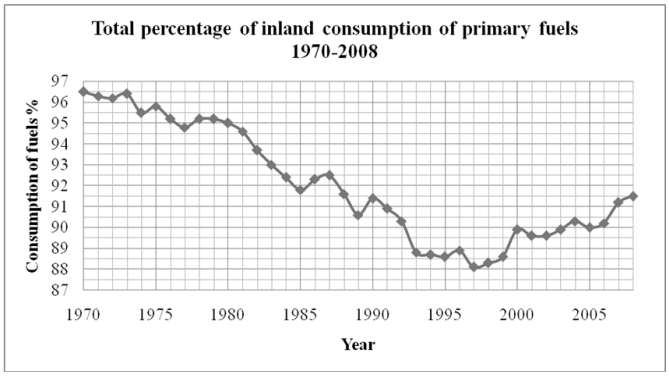

Figure 1: UK consumption (%) of primary fuels 1970-2008, data from [2]

The shape of wind turbine blade is just like the wings of an airplane and uses the airfoil shape to create life and maximize efficiency. The blade shape is so important that it influences blade efficiency and overall performance. In order to target high efficiency of the wind turbine performance, it is essential to optimise blade shape, number of blades, tower high and control system.

1.2 Wind Resources and Wind Energy

Wind is created as the circulation of the atmosphere due to uneven heating causes atmospheric pressure to move from high to low. This is because the distribution of solar energy radiated to the earths surface is different amount at the equator and the poles and this phenomenon causes the flow of air to rise at the equator and sink at the poles within the layer of troposphere. Hence this atmospheric flow makes the direction of pressure force in horizontal, which results in the same direction of the wind blow. At the same time, in addition to the pressure gradient force, inertia of the air, the earths rotation, gravitational force and friction with the earths surface, affect the atmospheric winds.

Wind energy has been controlled as power to ship and to power windmills which directly use the mechanical energy. Wind turbine however converts the mechanical energy to electricity. Wind is very friendly to economics and environment and has benefits of being clean, abundant and free.

The uses of small- and medium-size wind turbines has been growing and been in operation worldwide, especially in Denmark, Germany and the Netherlands. The capacity of wind turbine energy gradually grew from 10 kilowatts (kW) to 15 kW, then 30 kW since 1970s. This success encourages the wind energy industry to build wind turbines from 500 kW to 1.5 megawatts. Today those modern wind turbines in small and medium sizes are capable of meeting the residential needs of hundreds of homes. The global wind power installed in 2003 was over 8,000 MW bringing the total global wind power generating capacity to nearly 40,000 MW [3]. It is expected that the global market for wind power could reach 150,000 MW by 2012 [3]. Moreover the supplement of 10-12% of global electricity demand will be the target by 2020, which equals the 20% reduction of CO_2 emissions by 1.5 billion tonnes per year, defined by Global Energy Wind Council (GWEC) [4]. Figure 2 and Figure 3 show the amounts of electricity generated from wind and wave energy, and the compar-

ison to the total renewable energy during the period of 1990-2008. Figure 4 and Figure 5 show the contribution to wind power in different countries and regions. It can be seen from Figure 4 and Figure 5 that Europe was the world leading regional market and in fact that Germany is the number one market in wind power followed by the US [4].

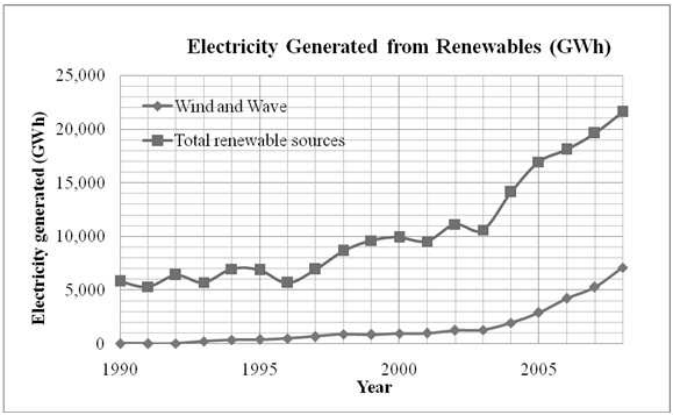

Figure 2: Electricity generated from renewable sources in the UK 1990-2008 [2]

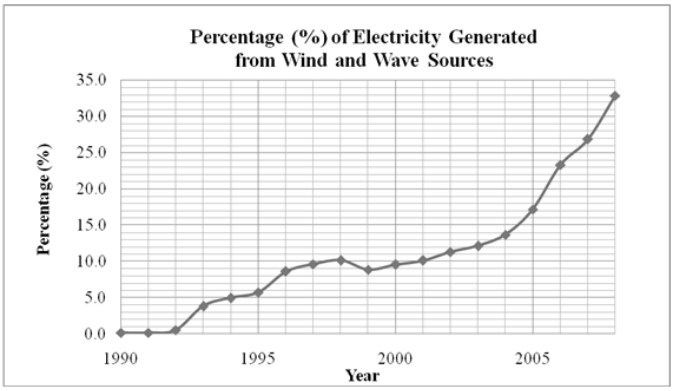

Figure 3: Electricity generated from wind and wave renewable sources in the UK 1990-2008 [2]

Wind is intermittent. This results in the main problem of wind power as wind power generation needs regular and strong in air flow. It must be either offshore or on mountain where is far away from the cities where the energy

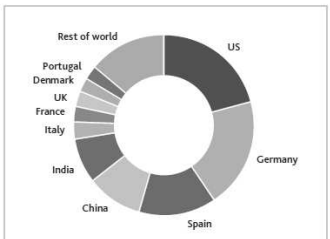

	MW	%
USA	25,170	20.8
Germany	23,903	19.8
Spain	16,754	13.9
China	12,210	10.1
India	9,645	8.0
Italy	3,736	3.1
France	3,404	2.8
UK	3,241	2.7
Denmark	3,180	2.6
Portugal	2,862	2.4
Rest of world	16,693	13.8
Total top 10	**104,104**	**86.2**
World total	**120,798**	**100.0**

	MW	%
USA	8,358	30.9
China	6,300	23.3
India	1,800	6.7
Germany	1,665	6.2
Spain	1,609	5.9
Italy	1,010	3.7
France	950	3.5
UK	836	3.1
Portugal	712	2.6
Canada	526	1.9
Rest of world	3,285	12.2
Total top 10	**23,766**	**87.8**
World total	**27,051**	**100.0**

Figure 4: (a) Total installed capacity and (b) New capacity in 2008 [4]

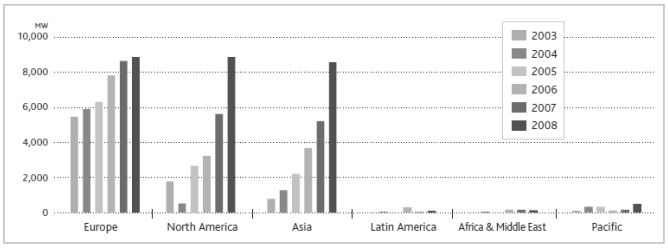

Figure 5: Annual installed capacity by regions between 2003 and 2008 [4]

is most needed. This makes however also some arguments against ruin of the natural landscape and threat to the birds.

It is important to determine the distribution of wind speeds because of the distributions considerable influence on wind potential. It is the annual mean wind speed at the site that is one of the main parameters in determining the economic viability of the wind project. In wind turbine manufacturers it is possible to calculate the amount of energy that the machine should capture annually with consideration of the performance characteristics of a specific wind turbine and the wind speed characteristics at the sites.

Wind speed depends on location, local topographical and round cover variations. Figure 6 shows the difference in wind speed, where two sites are very close but wind speed is significantly different.

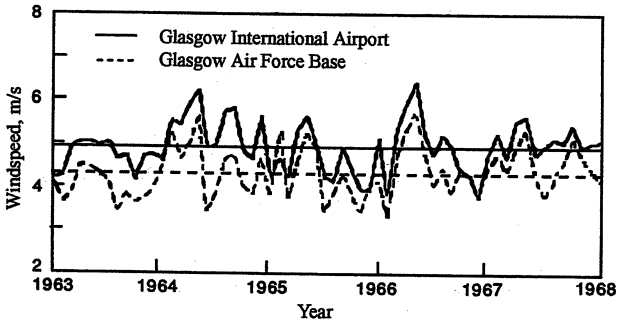

Figure 6: Time series of monthly wind speeds for Glasgow, Montana International Airport and Air force Base (AFB) [5]

1.3 Characteristics of Wind

As mentioned earlier in this report, the solar energy does not pour the same amount of radiation at the earths surface, greater at the equator and less at the poles. The difference of energy absorption presents uneven heat and in turn pressure difference, which makes the circulation of the atmosphere such as from the region of higher pressure to that of lower pressure. This is the wind.

In this section, the aspects that are considered in choosing and setting up a wind turbine at a location are listed and discussed.

1.3.1 Wind Speed Distribution

It is very important in wind energy to assess the statistical properties of the wind for prediction of wind energy output or speed and behaviour of a wind turbine. The most important property of the wind characteristics is wind speed distribution. This not only helps structural and environmental design and analysis but also assessment of the potential wind energy and the performance of wind energy system.

Direct and statistical methods are used for evaluation of wind resource and wind power production. Direct method is a way to calculate some useful

parameters such as average wind speed, average wind power density, average wind machine power and energy from a wind machine, from actual data of a given wind turbine at a given site where wind speed information is available in time series format. Statistical method however is used to determine the wind energy potential and the wind energy output at a given site. The requirement for probability distribution in statistical method is time series data at the desired location and height. In wind energy engineering, wind speed distribution is modeled using Weibull Distribution [5], which is based on two parameters, a shape factor and a scale factor and tells how often winds at different speed will be seen at a location with a certain mean wind speed. Rayleigh distribution is one of two probability distributions in wind data analysis using a parameter, the mean wind speed. Archer et al [6] describes their own methodology called he Least Square methodology that is focus on sound of flowing wind and surface of ground at locations to estimate the global wind power potential for identification of ideal sites for wind turbine operations.

Figure 7 and Figure 8 show Weibull distribution as examples. Figure 7 is a Weibull probability density function for various values of k and Figure 8 is typical wind speed probability and power curve of the Vestas V47-660kW. Appendix 5.1 includes the wind energy characteristics for Weibull distribution and all of the wind turbine characteristics [7].

1.3.2 Wind Variation in Time

Atmospheric motions vary in both time and space. It sometimes occurs in daily time scale large variation in wind speed due to differential heating of the earths surface during the daily radiation cycle. Daily solar radiation controls diurnal wind variation in temperate latitude over relatively flat land areas [5]. And it is said that the diurnal variation in wind speed may vary with location and altitude above sea level as the diurnal pattern may be different at altitude.

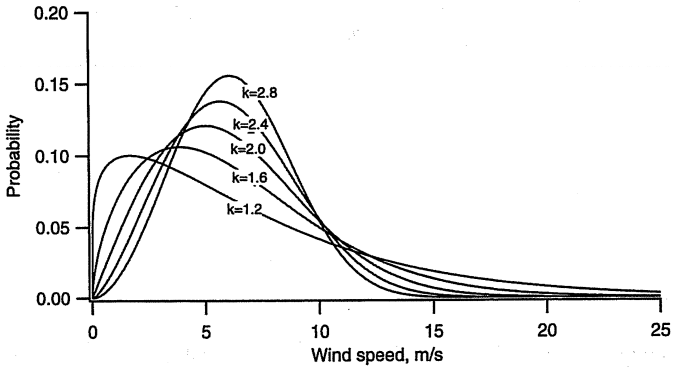

Figure 7: Example of Weibull distribution for the mean wind speed of 8 m/s [5]

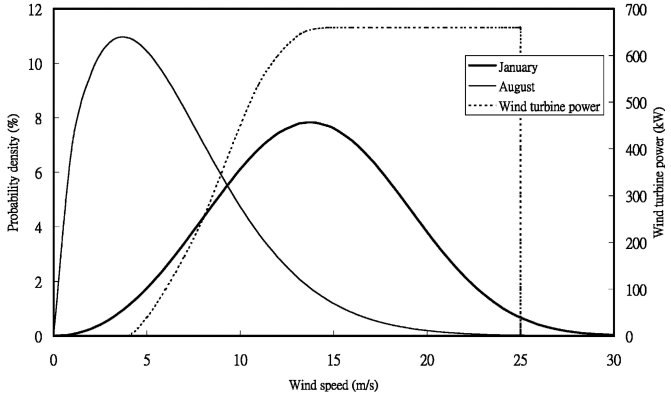

Figure 8: The performance curve of the Vestas V47-660kW turbine and typical wind speed probability in January and August in Taiwan [7]

Above all, for wind power application, it is required to quantify turbulent fluctuation in the flow in short-term wind speed variation over time intervals of 10 minutes or less. Turbulent flow encourages consideration for turbine blade design based on maximum load and fatigue prediction, control, system operation and power quality etc.

1.3.3 Wind Energy Power

Now the next step after analysis of wind data and wind characteristics is to determine wind turbine power production from wind data. The more detail of wind power is described in Chapter 2 in the text. Wind energy power

available is the power that flows at speed V (m/s) through wind turbine blade of sweep area A (m^2) in the air density of p (kg/m^3).

$$P = \frac{1}{2}\,\rho\,A\,V^3 \tag{1}$$

As it can be seen from the formula above that when the wind speed doubles, the power available increases by a factor of 8. This means hence that there is very little power available in low winds. In another words, wind energy power is proportional to swept area and the cubic of its velocity, it is important to consider stability in the property of wind speed. The wind power density is the wind power per unit area which is sometime called Weibull probability density and is used to determine locations with constantly high wind speeds. It can be expressed as follows.

$$\frac{P}{A} = \frac{1}{2}\,\rho\,V^3 \tag{2}$$

Here is an example to see the relation between wind speed and wind power density below. Figure 9 shows the average wind power for each hour for 3 days at a typical location. The average wind power density, $\frac{P}{A}$, based on hourly average, $\bar{V}$, is evaluated in quantitative magnitude of wind resource as poor in less than 100 W/m^2, good around 400 W/m^2 and great in more than 700 W/m^2 [5]. Hence it can be seen from Figure 9 that from hour 9 to hour 18 is appropriate for power production for this wind turbine at the location in the time duration. The data is included in Appendix 5.2.

1.4 Review of Current Small and Large Wind Turbines

There are a wide range of wind power turbine technologies available, from micro-scale to large commercial wind turbines. Small-scaled wind turbines are generally located where the power is required and such locations produce

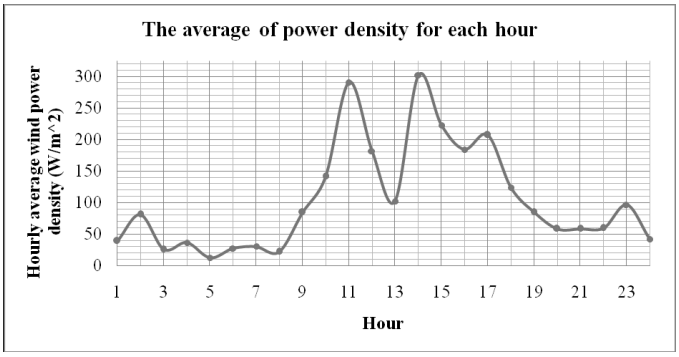

Figure 9: The average power density from hourlu agevage wind speed [8]

winds in short period and instability. On the other hand, commercial wind turbines are where the wind is most favourable. Wind turbines are also classed by the orientation of the axis of rotation to the direction of the wind. There exits two types: horizontal axis wind turbine (HAWT) and vertical axis wind turbine (VAWT). Majority of turbines in wind firms are horizontal-axis wind turbine (HAWT) and only 3% vertical-axis wind turbine (VAWT) [9].

1.4.1 Small Wind Turbines and Issues

The domestic small-scale wind turbines have been monitored in different area of 57 sites in the UK since 2007. These small wind turbines installed in ordinary peoples house generated as approximately 3,459GWh as UK hydro plants [10]. Especially free standing pole mounted turbines developed good records of performance across UK. This report from BWEA results in a potential UK renewable energy technology for development of small wind turbine system.

One of the issues on small wind turbines is low capacity factor in power. The wind in such circumstances under buildings and other adjacent obstructions for small turbines is normally weak, unstable and turbulent in wind speed and direction. Thus design of small turbine has to be improved to capture low wind speeds and to response quickly to turbulent wind resource areas.

1.4.2 Large Wind Turbines and Issues

The wind turbine capacity has increased from 100kW to 5MW by 2009 in commercial wind turbine. Turbines ranging from 1MW to 3MW are commonly used in industrial sites and on-shore wind firms. The reason behind the increasing capacity is the greater efficiency of the system and the improved economies of scale. A wind energy company, Multibrid Gmbh in Gerany, [11] succeeded in installation of 5MW wind turbine. Figure 10 shows how the scaled available wind turbines have increased over the past two decades.

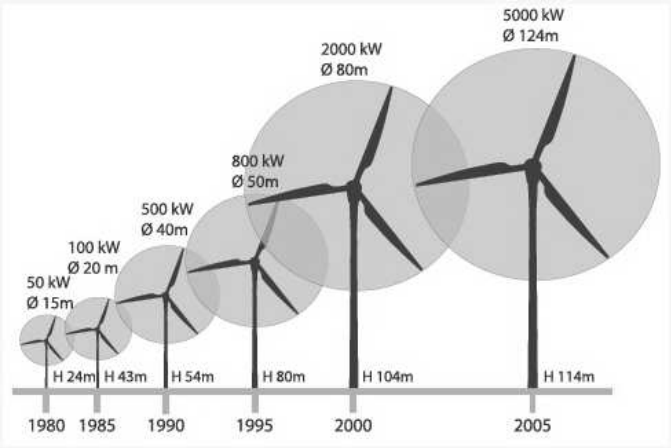

Figure 10: Growth in power and diameter in 2 decades [12]

For large-scaled wind turbine, it is a big challenge that the environmental impact of wind turbine should be minimized as most wind farms are required to consider all environmental aspects of wind energy projects. The common aspects are effects on wind power regularity, landscape, wildlife and sound generation. The installment of large-scale wind turbines has issues of the perceived intermittency of winds and the identification of good wind locations [6]. It is thought that the layout of wind farms does not disturb natural landscape although it has been improved to tubular tower and slender and refined nacelle shapes. The sound issue on wind turbine is generated by aerodynamic from the blades and mechanical from the rotating machinery. Ice accretion

is also concerned in cold climate conditions. In ice condition, it is discovered that lift decreases and drag increases as glaze is accumulated on the blade profile, which causes a negative torque and the stop of wind turbine [13]. The icing makes many other problems such as excessive turbine vibration, load imbalance, high fatigue load and increase of bending moment of blades. It is also true that larger rotor sizes restrict design margins for blade materials and structure to control the weight reduction. In fact, the increase in rotor size has not been accompanied by a cubic increase in blade weight [14].

1.4.3 Types of Wind Turbines

HAWT are made three-bladed and pointed into the wind to have high tip speed, high efficiency and low torque ripple for reliability. VAWT has on the other hand variety types of wind turbine; savonius, darrieus, giro mill and cycloturbine. These are foundations of modern type of VAWT and turby, quiet revolution and aerotecture are advanced to reduce torque issue by using the helical twist of the blades. VAWT are not pointed into the wind and the main rotor shaft runs vertically. HAWT and VAWT have several advantages and disadvantages as shown in Table 1.

1.4.4 Wind Turbine Industries

Table 2 shows the main wind turbine manufacturers worldwide which installed wind turbines in size of megawatts in 2007 [16]. The lists of size specification of common industrial wind turbines are in Appendix 5.3. Advertised wind turbines are rated by based of peak output power in high winds which are relatively rare.

Table 1: Advantages and disadvantages of HAWT

Advantages
Access to higher wind speed due to tall tower and hub used
Less ground space due to tubular tower
Great control due to adjustment of angle of attack
High efficiency since the blades face perpendicularly to the wind
Disadvantages
Difficulty in installation for tall HAWT
Difficulty in transportation, 20% of equipment costs [15]
Sound generation from blade tips and gearbox
Massive tower construction to support the heavy blades, generator and gearbox
Requirement of law control system to turn the blades to the wind

Table 2: Worldwide installed wind turbines in MW in 2007

Company	Country	Size of wind turbine (MW)
Vestas	Denmark	4500
GE Energy	United States	3300
Gamesa	Spain	3050
Enercon	Germany	2700
Suzlon	India	2000
Siemens	Denmark/Germany	1400
Acciona	Spain	870
Goldwind	China - PRC	830
Nordex	Germany	670
Sinovel	China - PRC	670

The worlds largest wind turbine is 6MW in height of 198m and diameter of 126m, manufactured by German company, Enercon (Enercon E-126) [17].

1.5 Scope of This Thesis

This project is the one that expands the project conducted by Professor. Alexanders PhD student, I.A.Hamakhan, in Queen Mary, University of London. It also expands on work previously done by MEng group, Rahman et al [83], with supervision of Professor. Alexander. The goal of my research is to identify the aerodynamic characteristics of blade over air flow and to find a geometry that maximize flow requirements. The main research was Computational Fluid Dynamics (CFD) review of the blade designed in Matlab by Professor Alexander and his PhD student.

2 Literature Review

2.1 Wind Turbine Design Procedures

This chapter presents a design procedure using aerodynamic characteristics for the rotor of a HAWT. The disc theory or actuator theory is widely used in the feature of the flow around the rotor or disc. After the assessment of aerodynamic calculation, the influence of the number of blades including solidity is considered on aerodynamic performance in numerical and experimental methods as well as advantages and disadvantages. It will show how unpopular wind turbines such as fewer blades and multi-blades are able to extract energy as much as wind turbines commonly used in wind turbine industry. Then the ideal performance is concerned by taking tip speed ratio into account, whose factor related to the rotor performance.

In order to see the variation of aerodynamic parameters along the blade, velocity vector diagram is introduced which displays the forces and velocities on the blade. The understanding of velocity diagram leads to the usage of Euler equation.

2.1.1 Disc theory

It is actuator disc approach that helps understand the power production process of the turbine, described in wind characteristics in Chapter 1. This approach was used to work on the flow through propeller by Glauert (1959) and windmill by Betz (1926) [3]. His contributions to wind turbine will be shown later on. This method helps understand the relation of the angles to a blade and chord length by deciding TSR, swept area, angle of attack and C_L.

As shown in Figure 11 below, the rotor of the horizontal axis wind turbine (HAWT) in the flow model is replaced by an actuator disc.

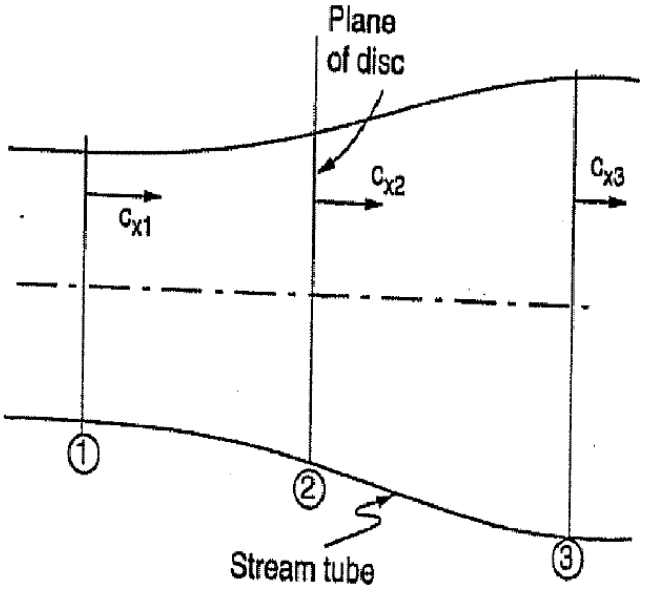

Figure 11: Actuator disc and boundary stream tube model [3]

As the flow approaches the actuator disc, the streamlines are diverted and its velocity is decelerated by a resistance of the disc to the air flow. There will be then a corresponding increase in pressure. On the other hand, the flow passing through the disc shows a sudden drop in pressure below the ambient pressure, which results in pressure discontinuity at the disc although there is a gradual recovery of the pressure to the ambient level in the downstream of the disc.

Now it is defined that axial velocities of the flow are as follows:

$$\text{Far upstream, } C_{x1}\text{: } x1 \rightarrow -\infty$$

$$\text{At the disc, } C_{x2}\text{: } x2 = 0$$

$$\text{Far downstream, } C_{x3}\text{: } x3 \rightarrow \infty$$

Also as simple assumptions concerning the flow, it is uniform and steady velocity upstream of the disc and at the disc, the flow around the disc is mixed both upstream and downstream by boundary stream tube, no flow rotation produced by the disc and it is incompressible flow.

From the continuity equation the mass flow at the disc is

$$\dot{m}_{x2} = \rho\, A_{x2}\, C_{x2} \tag{3}$$

Where ρ is air density and A_2 is area of disc.

The axial force acting on the disc is

$$X = \dot{m}_{x2}\,(C_{x3} - C_{x1}) \tag{4}$$

The corresponding power extracted by the turbine or actuator disc is

$$P = X\, C_{x2} = \dot{m}_{x2}\,(C_{x3} - C_{x1})\, C_{x2} \tag{5}$$

Now using the conservation of mass,

$$m_{x1} = m_{x2} = m_{x3} \tag{6}$$

The power output from the upstream and downstream winds is

$$P_w = \frac{1}{2}\dot{m}_x\,(C_{x3}^2 - C_{x1}^2)$$
$$P_w = \frac{1}{2}\dot{m}_x\,(C_{x3} - C_{x1})(C_{x3} + C_{x1}) \tag{7}$$

When $C_{x1} = C_{x3}$, then no power output is extracted. When $C_{x3} \approx 0$, then no power output is made as the mass flow rate is almost zero. Therefore C_{x3} exists in order to obtain the maximum power output between 0 and C_{x1}. This is done by knowing the value of C_{x2} at the disc.

When assuming that there is no energy loss, the power gained by the turbine or actuator should be equal to the power lost by the wind. Then

$$P = P_w \tag{8}$$

Comparing (8) with (5), the velocity at the disc can be obtained as follows.

$$C_{x2} = \frac{1}{2}\left(C_{x1} + C_{x3}\right) \tag{9}$$

This tells that the flow velocity at the actuator disc is the mean of the velocities far upstream and far downstream of the disc.

The following equation is obtained by inserting the mass flow rate at the disc and the velocity at the disc into the power output equation.

$$P = \frac{1}{2}\,\rho\, A_{x2}\, C_{x1}^{3}\, \left[\frac{1}{2}\left(1 + \frac{C_{x3}}{C_{x1}}\right)\, \left(1 - \left(\frac{C_{x3}}{C_{x1}}\right)^{2}\right)\right] \tag{10}$$

$$P = \frac{1}{2}\,\rho\, A_{x2}\, C_{x1}^{3}\, C_{p} \tag{11}$$

A power coefficient, C_P, is defined as

$$C_{p} = \frac{1}{2}\,\left(1 + \frac{C_{x3}}{C_{x1}}\right)\, \left[1 - \left(\frac{C_{x3}}{C_{x1}}\right)^{2}\right] \tag{12}$$

and also

$$C_{P} = \frac{Power\, Output}{Power\, Available} \tag{13}$$

Where the kinetic power available in the unperturbed wind at the disc is

$$P_{0} = \frac{1}{2}\,\rho\, A_{x2}\, C_{x1}^{3} \tag{14}$$

The maximum value of C_P under theoretical ideal conditions is 0.593, which is referred to as the Betz limit. It is possible to obtain a value of C_P from 0.3 to 0.35 for most machines of good design [3]. Johansen et al [18] obtained maximum aerodynamic efficiency in a certain operational condition by using actuator disc model. Figure 12 shows the gap of wind power output between

theoretical calculation and experimental data. The data is of Vestas V90-3.0 MW in Appendix 5.4. The results bring the values of C_P from 0.05 at 25 m/s to 0.5 at 5 m/s.

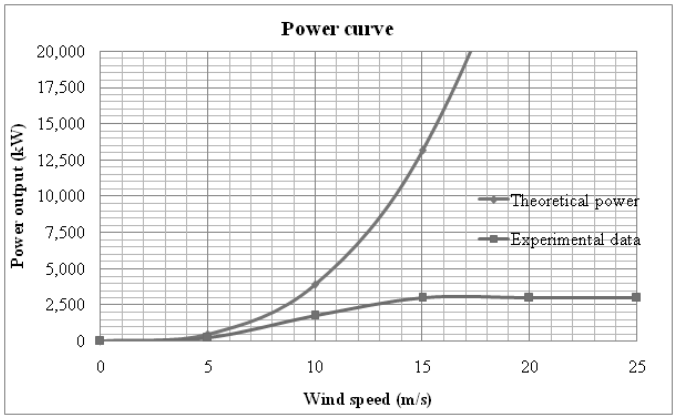

Figure 12: Example of power curve [19]

It is thought that the reductions of drag generated on the blade geometry and of pressure difference at the tip of the blade between suction side and pressure side moderate low efficiency of the blade performance [1].

The idealized power curve for a wind turbine is shown in Figure 13 The curve in the graph derives from the power available equation, where is between the cut-in wind speed and the rated wind speed. Where the cut-in wind speed is the speed at which the turbine starts to generate power and the rated wind speed is the speed at which the maximum power is first reach. Once the power output reaches the maximum point at the rated wind speed, it stays constant beyond the wind speeds and then the rotor brakes to rest at the cut-out wind speed which is the maximum permitted wind speed.

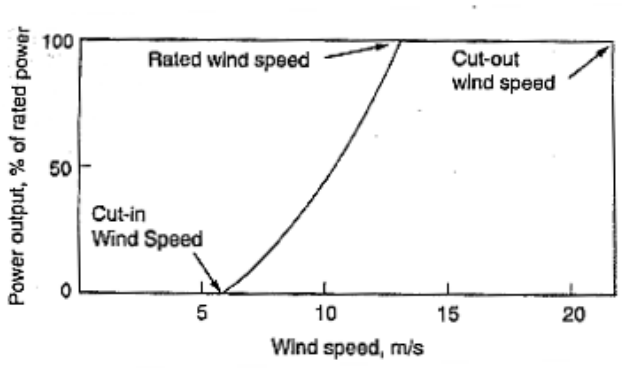

Figure 13: Idealized power curve for a wind turbine [3]

2.1.2 The effect of the number of blades

Since Betz limit was introduced in wind turbine energy, which provides the maximum power coefficient is about 59%, many designs in HAWT and also VAWT have been examined and improved that they hardly reached the Betz limit.

Effect of the number of blades is considered in aerodynamic performance on wind turbine such as tip-speed ratio and power coefficient as well as other factors such as weight, cost, fatigue life and structural dynamics. Also it is indicated by Tangler [20] that the choice of blade number supports the consideration of rotor noise. In wind turbine industry, three-bladed rotor in upwind is more preferable than two-bladed rotor in terms of better balance among blade stiffness, aerodynamic efficiency, vibration and noise even though fewer-bladed wind turbine design saved the cost of rotor blade and its weight. However in terms of efficiency, it was examined by Duquette and Visse [21] that 12-bladed rotor makes 44% efficiency.

Figure 14 shows performance comparison of power coefficient versus tip speed ratio (TSR) for wind turbine designs obtained by Johnson [22]. The more detail of TSR is described later in the next section. It can been seen from Figure 14 that two-blade turbine hits the highest power coefficient in

the range of 4 to 7 in tip speed ratio, which is closer to the Betz limit.

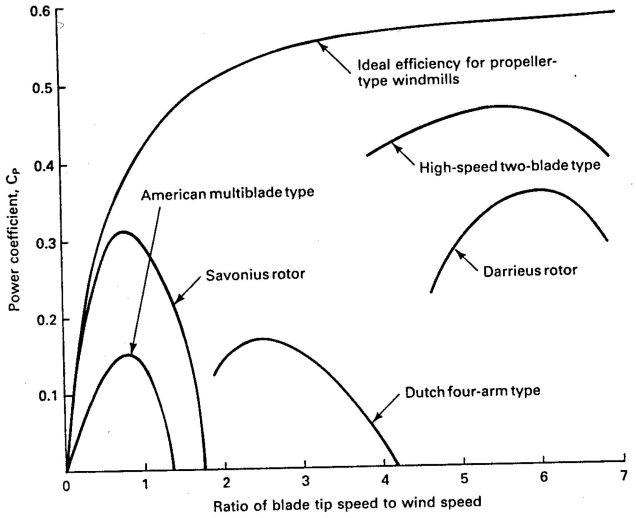

Figure 14: Typical performances on five different turbine machines [22]

Figure 15 is another graph to show increase in aerodynamic efficiency in y axis with increased blade number, 1 to 4 blades and tip speed ratio in x axis. It is discovered that the blade number from one to three results in approximately 9% increase in aerodynamic efficiency. Further blade number however makes imbalance in stiffness which causing to minimize increase in aerodynamic efficiency.

The interaction between wind and blades are complicated but the solidity of a given rotor tends to reduce the incoming wind speed to wind turbine blades and then sacrifice the use of wind energy. In turn the wind speed determines the blade configuration.

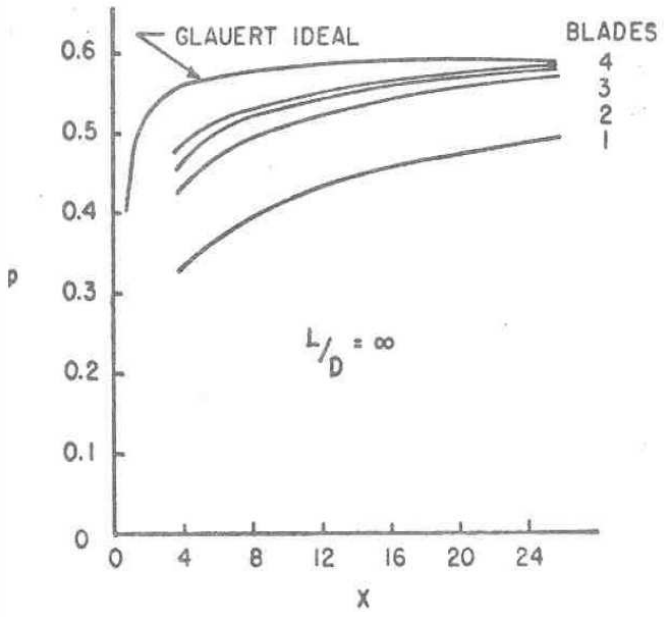

Figure 15: Aerodynamic efficiency vs tip speed ratio as increase of blade number [20]

Two and three-blade turbines

As shown earlier in this chapter, the majority of wind turbines today are three blades. One of the reasons behind the fact is higher fatigue loads and noise problems in the past years of wind turbine history. To overcome this issue in two-blade turbine, it is necessary to increase blade chord, which brings thickness to chord ratio for the structural requirements of the blade. The focus is on keeping the total area of active surface in aerodynamics to achieve a specific wind braking effect. As the blade thickness increases the blade chord increases. Hence the thicker blade increases strength, relatively remains lighter and cheaper without additional structural materials. It is expected as a result of longer blade chord and stronger blade that the blade tip speed which is hence rotational speed will be obtained larger values. Figure 16 shows yearly energy production in two-bladed turbine, comparing with three-bladed turbine, surveyed in wind turbine company, Nordic Windpower [23]. It is noted that the difference between them is 2-3% of energy production in

year. This concludes that todays two-bladed wind turbines are designed to produce as much tip speeds and energy as three-bladed wind turbines which leads less sound generation than before.

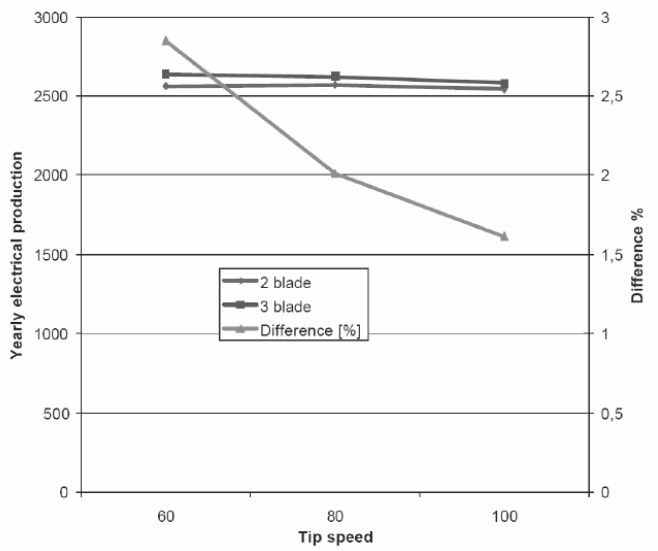

Figure 16: Yearly energy production from two- and three-bladed wind turbines [23]

Two-bladed wind turbine has an advantage in erection procedure as well as less cost and weight as the blades could be mounted to the nacelle on the ground. On a three-bladed turbine, on the other hand, the nacelle and blades have to be lifted separately to mount them at top of the tower.

It is harder to design asymmetrical two-bladed turbine than symmetrical three-bladed turbine. Two-bladed turbine concept requires a teetering hub to minimize heavy shocks to the turbine when a rotor passes the tower and an additional shock absorber to the main shaft to prevent the rotor from hitting the tower.

Multi-bladed turbine

Clarkson University found the results that in small size of HAWT aerodynamic performance is directly related to solidity and blade number [5]. The

results from his experiment tell that the more blade number and solidity, the greater power coefficient and both of factors contribute to the added torque that improves cut-in wind speed. Figure 17 displays that 12 blade rotor (B = 12) can make more significant power extraction than 3 bladed rotor (B = 3) which is commonly use in wind turbine industry. At solidity of 0.27 (σ = 0.27) the power coefficient of 12 blade rotor is 30% higher than that of 3 blade rotor. This result obtained numerically with the Expanding Wake Method (EWM) and lifting line theory by Gould and Fiddes [24]. However the wind tunnel experiments did not show the same results as the numerical results regarding increased blade number but solidity.

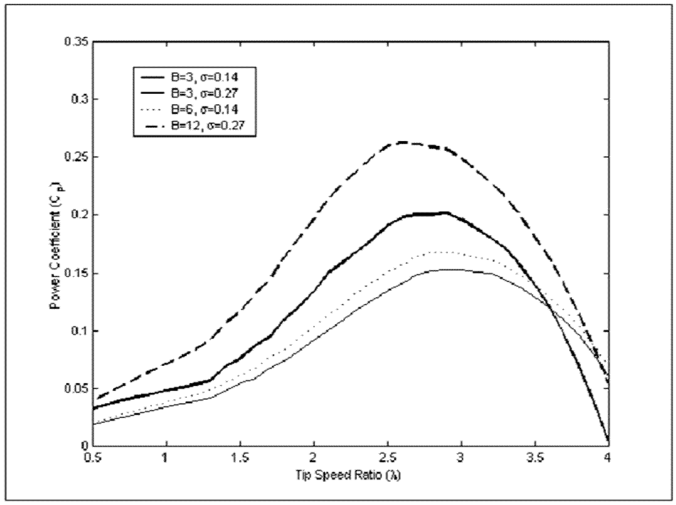

Figure 17: Characteristics of the effect of blade number and solidity in numerical results of EWM [24]

2.1.3 Tip Speed Ratio (TSR)

TSR is the ratio between the rotational speed of the tip of the blade and the actual velocity of the wind and described as lambda, λ. TSR is a factor that directly affects the energy generated from the turbine. The relation between TSR and power coefficient for different types of wind turbines are shown in Figure 14 and 15.

TSR determines how fast the wind turbine will rotate and generally depends on the particular wind turbine design used, the rotor airfoil profile used and the number of blades used. For example, TSR in three blade turbines ideally drops between 6 and 8. Although the higher TSR is the better, the turbine will generate noise and mechanical stress at some point in TSR range. Little power extraction will be made in slow rotation of the rotor since the wind pass through the gaps between the blades without distribution. Also little power extraction will be made in fast rotation of the rotor due to solidity causing the wind flow to be obstructed. It is therefore important for wind turbine designers to make wind turbines operate in the range of their optimal TSR by considering the relation of angular velocity and wind speed in order to extract as much power as possible from the wind stream.

$$TSR = \frac{Rotational\, speed\, of\, the\, tip\, of\, the\, blade}{Actual\, velocity\, of\, the\, wind} \tag{15}$$

$$\lambda = \frac{\omega\, r}{C_x} \tag{16}$$

Where ω is angular velocity, $2\pi f$, (rad/s), r is rotor radius (m), C_x is wind speed (m/s) and f is frequency of rotation (Hz, rpm, $1/s$).

Now the optimal TSR is a tip speed ratio when maximum power is extracted from the wind, which can be described as the time taken for the disturbed wind to re-established itself, t_w equals to the time taken for a rotor blade of rotational frequency to move into the position occupied by its predecessor, t_s. Hence for an n blade rotor,

$$t_w = t_s \tag{17}$$

$$\frac{S}{C_x} = \frac{2\,\pi}{n\,\omega} \tag{18}$$

Where S is length of disturbed wind (m), C_x is wind speed (m/s) and n is number of blade. Now if $t_w < t_s$, some wind is unaffected and if $t_w = t_s$, some wind is not allowed to flow through the rotor.

Hence the optimal angular velocity of the rotor is obtained from the equation above as

$$\omega_o pt = \frac{2\,\pi\,C_x}{n\,S} \tag{19}$$

The optimal TSR is

$$TSR_o pt = \frac{\omega_o pt\,r}{C_x} \tag{20}$$

$$\lambda_o pt = \frac{2\,\pi\,r}{n\,S} \tag{21}$$

It was empirically observed in the wind energy industry that the length of disturbed wind, S, is approximately half a rotor radius, r, which gives the optimal TSR as follows.

$$\lambda_o pt = \frac{4\,\pi}{n} \tag{22}$$

For two bladed rotor,

$$\lambda_{opt,2} = 6.283 \tag{23}$$

For three bladed rotor,

$$\lambda_{opt,2} = 4.189 \tag{24}$$

Table 3 shows how wind speed, blade rotation per minute and blade size can affect TSR. For a given rpm, TSR increases as rotors speed increase or

as the length of the blade increase. It can be seen from the table below, in the case of unfixed rpm, that on PVC Geared Turbine, three different wind speeds have several TSRs which are all under optimal number of TSR for 3 blade rotor. The small size of rotor such as BWC Excel which has three blades obtained very high TSR which is about twice of the optimal TSR for three bladed rotors.

Table 3: TSR measurements in several wind turbines in different size and blade number, [25]

Wind turbines	Diameter (m)	Blade number	Wind speed (m/s)	rpm	TSR
PVC Geared Turbine	0.432	3	4.4	750	3.9
			3.8	520	3.1
			2.9	380	3.0
BWC Excel	7	3	14	310	8.2
Vestas V47	47	3	15	26	4.3
Bonus 1MW/54	54	3	15	22	4.1
Monopteros 50	56	1	11	43	11.0

2.1.4 Euler equation and velocity diagram

Euler equation is well-known to govern inviscid flow in fluid dynamics and is widely applicable in compressible and incompressible flows. This is a different way from the disc theory to describe power output from wind turbine blades in that work transfer from the fluid through the rotor are considered to produce change in enthalpy by taking three components of force acting to a disc. The following process and Figure 18 show how Euler equation is derived from energy transfer.

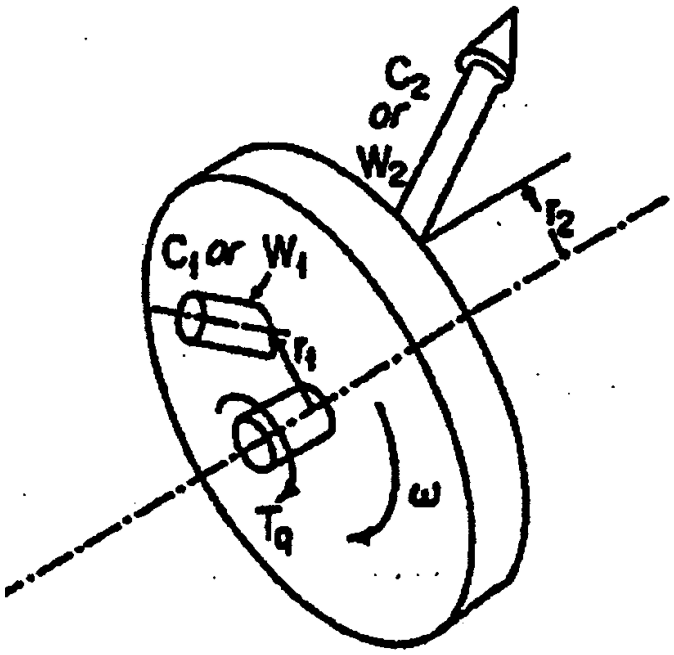

Figure 18: Flow through a disc [26]

In Figure 18 , absolute velocity is C, relative velocity is W, radius at which the flow enters the rotor is r, torque is T_q and angular velocity is ω. The subscripts 1 and 2 are inlet and outlet respectively.

The torque on rotor through incoming and outgoing flows is

$$T_q = \dot{m}\,(r_1\,C_{u,1}\;-\;r_2\,C_{u,2}) \tag{25}$$

Now using energy (E) is equal to torque times angle (in radians),

$$E = \dot{m}\,(r_1\,C_{u,1}\;-\;r_2\,C_{u,2})\,\omega \tag{26}$$

and rotor speed (u) is referred as angular velocity times the distance at which the flow enters the rotor, $u = \omega\,r$.

$$\dot{W} = \dot{m}\,(u_2\,C_{u,2}\;-\;u_1\,C_{u,1}) \tag{27}$$

Where $\dot{W}$ is power per second (W/s), $\dot{m}$ is mass flow rate (kg/s), u is rotor velocity ($m.rad/s$) and C with subscript u is tangential component velocity (m/s). Since the tangential component velocity at inlet of a wind turbine blade is zero,

$$\dot{W} = \dot{m}\,u_2\,C_{u,2} \tag{28}$$

The rotor velocity, u, is $\omega\,r$, ω is angular velocity (rad/s) and r is distance from the centre of rotor to the point the flow enters (m) and the work output is referred as below.

$$\dot{W} = \dot{m}\,\omega\,r\,C_{u,2} \tag{29}$$

Velocity diagram is a vector diagram that shows the velocities and fluid flow through blade rows. Velocity diagram can graphically display the velocities at the rotor inlet and outlet in the turbine, which relate to Euler equation. Examples of velocity diagram for axial-turbine and three blades HAWT are shown as follows.

In the velocity diagram in Figure 19 , C is absolute velocity; subscripts 2 and 1 describe the flow velocity into and out of the nozzle respectively. W is relative velocity; subscripts 1and 2 are into the rotor and out of the

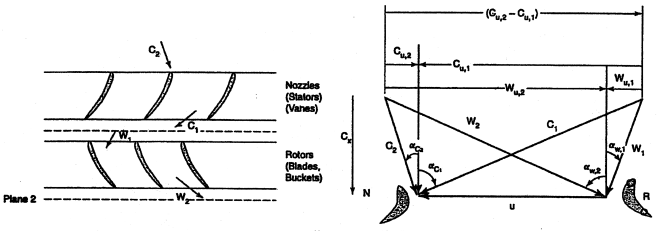

Figure 19: Axial-turbine stage blade rows and velocity diagram [26]

rotor respectively. Subscript u represents the tangential velocity component; corresponding flow angle ; the axial flow through the stage C_x; and the rotor velocity for the stage u. For a given rotor speed, the corresponding work output $\dot{W}$ is obtained by finding a tangential velocity, $C_{u,2}$, in the velocity diagram.

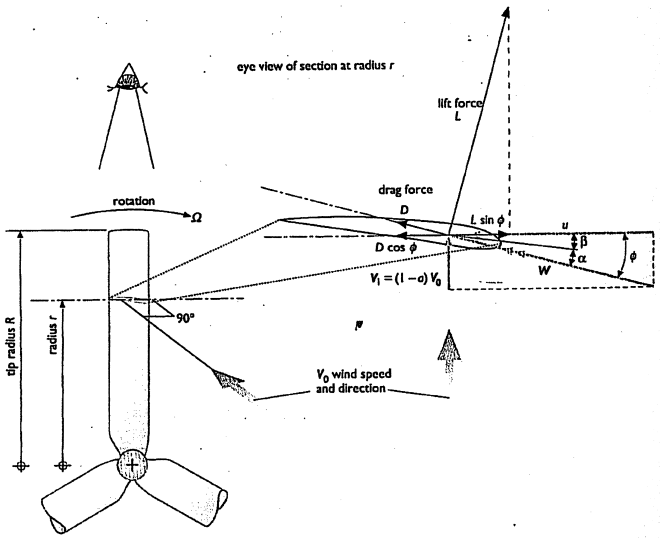

Figure 20: Velocity vector diagram of a moving rotor blade of a HAWT [27]

The velocity diagram of Figure 20 shows: the angular velocity Ω , the angle of attack α, the blade pitch angle β, the relative wind angle or flow angle ϕ, the relative wind velocity W, the wind velocity at the rotor V_1, the undisturbed wind velocity upstream of the rotor V_0 and the axial interference factor a that takes account of the wind being slowed down as a result of power extraction.

Since the rotor speed is equal to the angular velocity of the rotor times the

local radius, the relative wind angle or flow angle varies at the local radius along the length of the blade. It can be seen in Figure 21 below that the flow angle ϕ increases as the rotor speed u decreases.

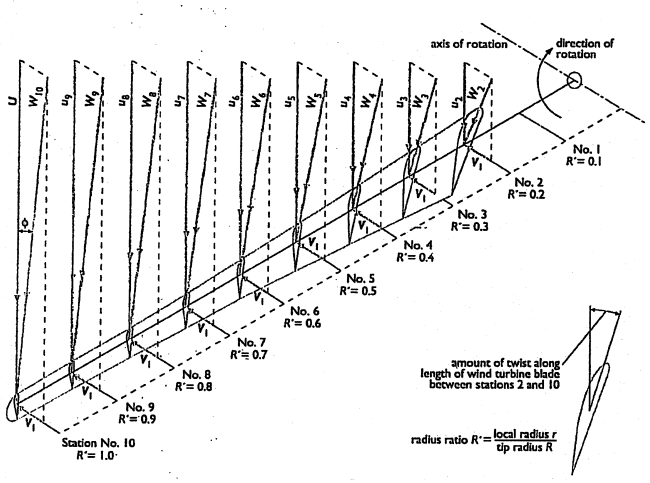

Figure 21: Changes of flow angle ϕ along the blade span of HAWT [27]

2.2 Wind Turbine Blade Design

2.2.1 Direct surface curvature distribution blade design method

In the design of blade, the minimum flow separation on blade surface is required since flow separation shows blade performance in the forms of pressure and velocity distributions of the blade surface as published, for example, by E.A.Mayda [28]. The flow separation occurs at the point of discontinuity on the blade surface and therefore blade surface distribution is concerned for curvature continuity. In order to obtain well-smooth surface curvature, a series of parameters of blade geometry is defined in a geometric description package and the performance of pressure distribution is analyzed through successive iterations in an analysis code such as ANSYS. This is called direct method for design of blade surface curvature distribution. The direct method is good in display of curvature shape but is handful of control in geometric parameters.

The surface curvature distribution is analyzed in smoothness by continuity in the curvature of the blade surface and the slope of curvature. This is because Korakianitis [29] reasoned from his works in the past years that a little change of the slope of the curvature of the blades affects the blade aerodynamic performance. He concluded that the concept of surface curvature distribution results in improvement of blade design and aerodynamic performance with prevention of flow separation and with smooth Mach number and pressure distributions.

The derivation of curvature distribution is from the Navier-Stokes equations of cylindrical coordinates in compressible flow. It shows the domination of local pressure and velocity on the curvature as well as on the slope of the curvature as explained in Equations (1), (2), (3) and (4) of Korakianitis [30]. Pressure and velocity distributions have an important role on the turbine blade design as the boundary layer close to the blade is dependent on the slope of the velocity distribution, which demands the blade performance. Smooth curvature distribution for velocity distribution therefore requires continuous curvature and the slope of the curvature along the blade surface for $y = f(x)$.

$$C = \frac{1}{R} = \frac{y''}{[1 + (y')^2]^{\frac{3}{2}}} \tag{30}$$

$$C' = \frac{dC}{dx} = \frac{y'''[1 + (y')^2] - 3\,y'\,(y'')^2}{[1 + (y')^2]^{\frac{5}{2}}} \tag{31}$$

Where C is curvature and R is local radius of curvature.

As it can be seen from the equations above that $y = f(x)$ is a third-order polynomial and has continuous first, second and third derivatives, which computes the curvatures of the trailing edge region of the suction and pressure sides.

The discontinuity in the slope of curvature causes unnecessary loading along

the blade and flow separation. It is very difficult to see any discontinuities in the designed curvature shape but the fluctuations in pressure coefficient and Mach number on the blade surface is visible in the form of spike as published in Sharma et al [31]. The availability of direct curvature method is reliable as observed by Korakianitis [30]. Korakianitis tested turbine blades in calculations of direct curvature distribution using computer program UNSFLO by Gile and compared them with the results of Euler computation and hodograph solution by Hobson.

Hamakhan and Korakianitis [32] designed blades consisted of three parts; trailing edge segment, main part and leading edge segments, which they concluded no flow discontinuities due to surface curvature discontinuities. The blade segment and structure which were arranged by [32] are shown in Figure 22. An airfoil consists of 6 segments: trailing edge suction side (TESS), main Bezier suction side (MBSS), leading edge suction side (LESS), trailing edge pressure side (TEPS), main Bezier pressure side (MZPS) and leading edge pressure side (LEPS). The trailing edge circle (TEC) and leading edge circle (LEC) are designed within the parts of TESS and LESS respectively. In the study of this project, the blade design programme was given to input main parameters of a blade as shown in Figure 23 and 24.

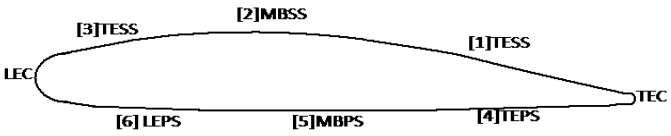

Figure 22: Airfoil segments [33]

The trailing edge part is structured by considering a circle at the edge and thickness distribution of the blade from the trailing edge to the main part [34]. The latter depends on the size of the radius of the circle. The equation of $y = f(x)$ used in the trailing edge segment which is from the trailing edge circle to the joint point (P_{s2}) to the main part is an analytic polynomial as

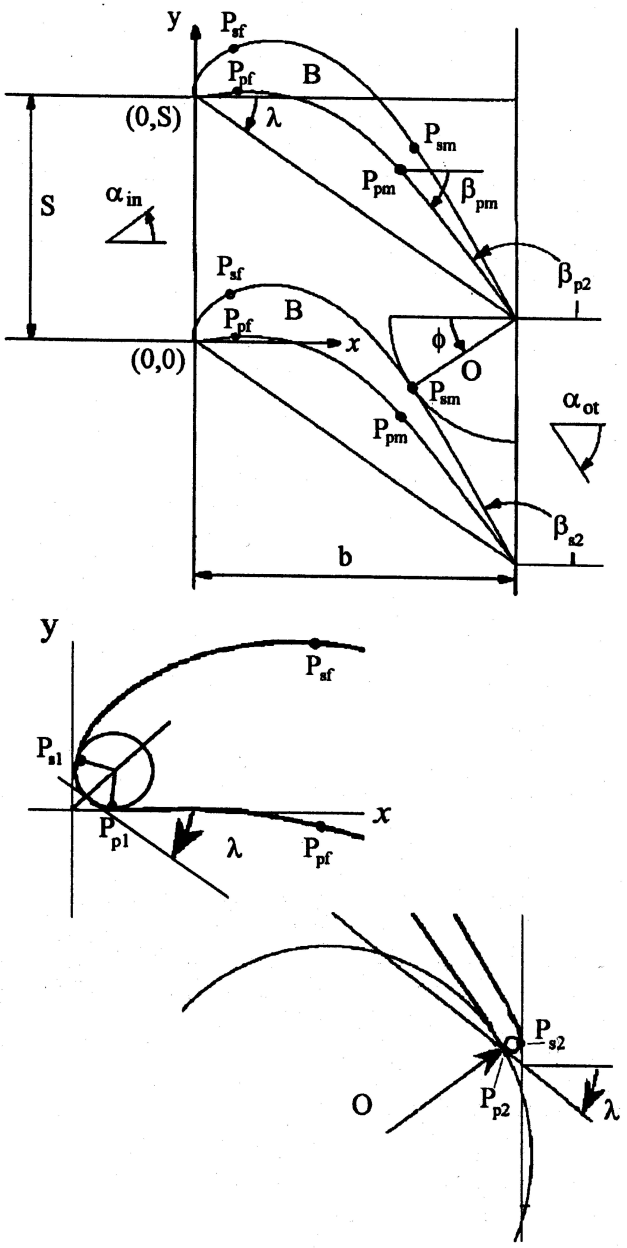

Figure 23: Illustration of 2D blade design method [34]

follows.

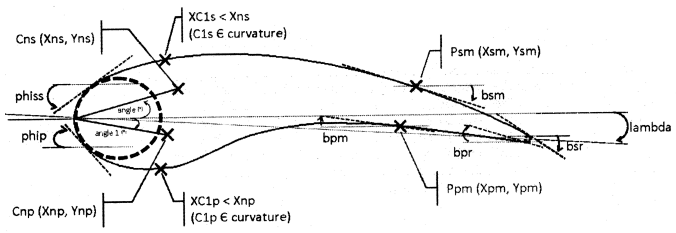

Figure 24: Airfoil structure [35]

$$y\left(x\right) = a_0 + a_1\, x + a_2\, x^2 + a_3\, x^3 + a_4\, k_1\left[x - x\left(P_{s2}\right)\right] + a_5\, k_2\left[x - x\left(P_{s2}\right)\right] \quad (32)$$

Where a is a parameter, k is exponential function and P_{s2} is blade surface point in suction side.

The main part is specified by its curvature distribution called Bezier curve which consists of five segments controlled by six points $C_{1s} - C6s$. The Bezier equation is on the plane of (C, y) which derives from the plane of (x, y) and is shown as follows.

$$\begin{aligned} x\,C = {} & t^3\, x\, C_{1s} \;+\; 3\, t^2\,(1-t)\, x\, C_{2s} \;+\; 3\, t\,(1-t)^2\, x\, C_{3s} \\ & + (1-t)^3\, x\, C_{4s} \;+\; (1-t)^4\, x\, C_{5s} \;+\; (1-t)^5\, x\, C_{6s} \end{aligned} \quad (33)$$

$$\begin{aligned} y\,C = {} & t^3\, y\, C_{1s} \;+\; 3\, t^2\,(1-t)\, y\, C_{2s} \;+\; 3\, t\,(1-t)^2\, y\, C_{3s} \\ & + (1-t)^3\, y\, C_{4s} \;+\; (1-t)^4\, y\, C_{5s} \;+\; (1-t)^5\, y\, C_{6s} \end{aligned} \quad (34)$$

This part is connected the trailing edge segment and leading edge segment of the blade. Figure 25 shows an example of curvature distribution on the suction side of the blade.

The leading edge has significant conditions on flow separation, pressure and Mach number distribution and hence a parabolic construction line and

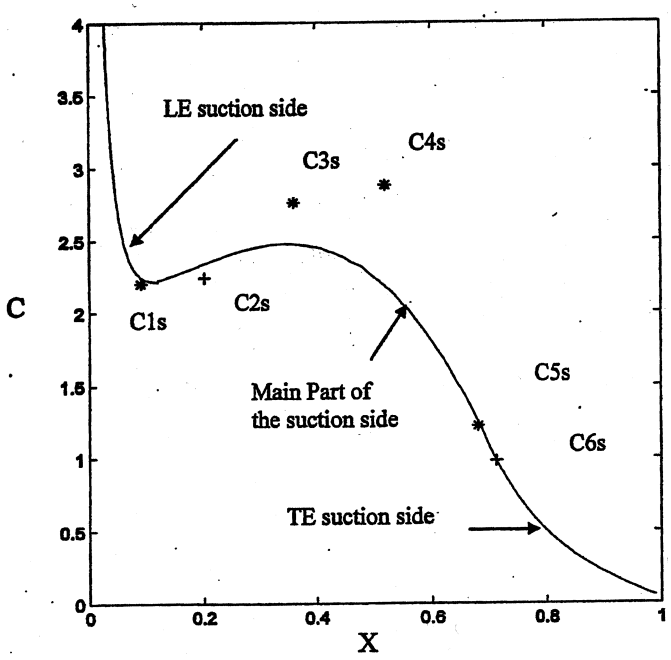

Figure 25: Example of curvature distribution on the suction side [32]

thickness distribution is inserted as well as a circle at the leading edge. The parabolic construction line passes through the leading edge from the centre of the leading edge circle and is specified by the angle of the construction line at the origin and of a point on the construction line.

$$y\left(x\right) = A\,x^2 \,+\, B\,x \,+\, C \tag{35}$$

Where A, B and C are constant.

The thickness distribution is added perpendicularly to the parabolic construction line and has continuous slope of curvature, $C^{'}$, which means first, second and third derivative in the following equation, at the tangent points of the circle and the main part of the blade.

$$\begin{aligned} y\left(x\right) = a_0 \,+\, a_1\,x \,+\, a_2\,x^2 \,+\, a_3\,x^3 \,+\, a_4\,k_1\left[x \,-\, x\left(P_{s1}\right)\right] \\ +\,a_5\,k_2\left[x \,-\, x\left(P_{sk}\right)\right] \,+\, a_6\,k_3\left[x \,-\, x\left(P_{s1}\right)\right] \,+\, a_7\,k_4\left[x \,-\, x\left(P_{sk}\right)\right] \end{aligned} \tag{36}$$

Where a is a parameter, k is exponential polynomial function, P_{s1} is joint point with the leading edge circle and P_{sk} is joint point with the main part of the blade.

2.2.2 Other design methods

It is true that most of the wind turbine blades have been designed in traditional inverse methods due to the extended computational possibilities [36]. The inverse method is defined as the blade geometry found in a prescribed pressure distribution at specified operational conditions while the direct design method is opposite to this approach as shown in Figure 26 and Figure 27. Therefore it is more dependent on direct interaction with the blade pressure distribution and less computational effort while direct methods relies heavily on the experience of the designer in the achievement of a target pressure distribution.

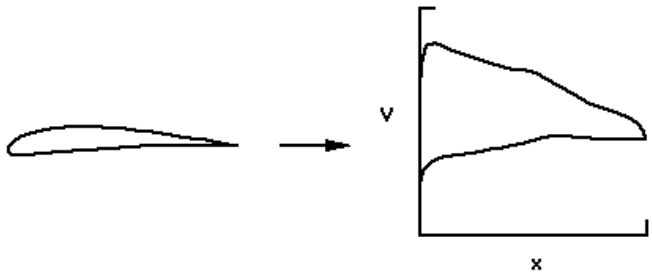

Figure 26: Direct design method to airfoil [47]

Direct design method includes momentum theory (BEM) and vortex wake method which require airfoil data in turbulent flow and geometry specifications such as blade spanwise chord distribution to calculate aerodynamic loads. Ameku [37] and Vitale [38] showed a potential way of analysis of blade performance and stability by using blade element and momentum theory (BEM) which allows to control seven arcs over a blade and to input desired

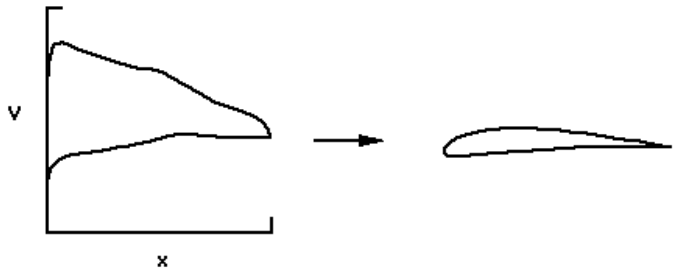

Figure 27: Inverse design method to airfoil [47]

aerodynamic values for wind turbines into the software called Zeus Disenador which designs horizontal-axis wind turbine blades with an iterative algorithm respectively.

There are mainly three types of solutions of inverse deign problem: pure inverse formulation methods, iterative use of analysis codes, optimization techniques. The pure inverse design methods determines directly the blade geometry of the blade section that achieves the specified desired flow conditions by input of the parameters of the desired flow conditions in a problem formulation as described earlier. The iterative use of analysis method is a geometry modification algorithm and solves numerically the time dependent Euler equation or Navier-Stokes equation to obtain a prescribed pressure distribution until reaching convergence. It determines the mean tangential velocity along the chord and thickness distributions as design variables. Henriques et al. [39] applied the inverse design method to design a high-loaded small wind turbine blades by considering the pressure difference between both sides of the blade section which is derived from the tangential velocity distribution which is directly related with the blade load. Pascoa et al. [40] show the improvement of the convergence rate and the robustness of the method by introducing a new blade thickness distribution term. De Vito et al. [41] developed iterative approach in viscous flow that the 2D-design of turbine blades with inverse method at transonic and supersonic flows can be used to

a large range of applications such as both turbomachinery blade and wings, following by Leonard et al. [42] and Demeulenaere et al. [43], who devised an inverse method in invscid flow based on Euler solver which solves a prescribed pressure distribution on the whole blade surface from the 3D-geometry definition. The optimization technique is different from the iterative use of direct approach by [41], [42] and [43] in usage of static pressure distribution but similar to iterative approach in specification of the mass-averaged tangential velocity and the thickness distribution. Tiow et al. [44] show that the inverse design method coupled with optimization technique can directly control the blade pressure loading which leads to limit shock losses in transonic and supersonic flows but not directly control the specific work.

Battisti [45] examined rotor arbitrarily radial load distribution, the wake rotation and expansion using inverse design method with vortex flow distribution and energy and momentum conservation, to apply a flow analysis of axial turbomachines with the assumptions that the applications to vortex distribution and boundary condition is equal to that to velocity distribution. It was concluded that the approach obtained a target design by controlling the spanwise mass distribution and the loads on the blade and hence was reliable and produced a realistic bade layout. Kamoun [46] presented optimisation of wind turbine blade geometry for a prescribed distribution of bound vortices using an inverse design procedure. This was done by accepting thickness and loading distributions of the blade section. The success of optimal circulation of bound vortex was assessed by the lifting strip theory.

Performance analysis of wind turbine is critical to design of a blade, which is concluded from the past experiences of wind turbine designers who thought that a small difference in aerodynamic performance of a blade does not affect the performance of wind turbine and they made more effort on optimisation in blade twist and taper. Therefore it was shortage of research on airfoil selection. Since then, airfoil has been aware of and designed to meet a target

performance in aerodynamics.

2.2.3 Design method in airfoil series

HAWT blades have been designed using airfoil families. NASA LS(1), NACA 44xx and NACA 63xx were common use in HAWT. However they suffer performance degradation from roughness effects resulting from leading edge contamination [39] [48]. The NACA airfoil series in 4 digits was geometrically designed using analytical equations that describe the camber (curvature) of the mean-line (geometric centerline) of the airfoil section as well as the sections thickness distribution along the length of the airfoil. It is believed that the 6-digit airfoil series designs are more theoretical than geometrical and more complicated by modifying to add some variables. Figure 28 shows the geometrical construction of NACA airfoil.

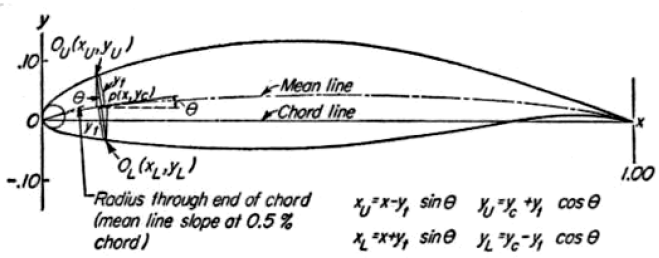

Figure 28: NACA airfoil geometrical construction [49]

The National Renewable Energy Laboratory (NREL) has overcome the energy losses when NREL started working to provide several series of airfoil for wind turbines in the 1980s with an effort of Tangler and Somers [48]. It exits nine airfoil families designed for various sizes of rotor using the Eppler airfoil design and analysis code. The requirement of the airfoil families performance is to maximize life coefficient which is relatively insensitive to roughness effects. It is reported in [48] that the NREL airfoil families have made improvement in annual energy production in several types of wind turbine blades.

RISO has developed the design of three airfoil families, Riso-A1, Riso-P and Riso-B1, for rotor size from 600 kW to MW in the middle 1990s. RISO-A series is designed by a direct method of a numerical optimization algorithm of a B-spline representation of the airfoil shape [36] [50]. This method showed insensitiveness to leading edge roughness in RISO airfoil series.

2.3 Aerodynamic Calculations and its Methodologies

The blade-element theory, originally developed for aircraft propellers by Froude in 1878 and Taylor in 1893, assume that the forces on the blade elements can be determined from the local flow conditions which are estimated by either momentum or vortex, or both, and the corresponding two-dimensional wind-section data. The blade-element theory can be applied to wind turbine. Then this approach was modified by several researchers such as Glauert in 1935 [51] [52] and Wilson and Lissaman in 1974 [53].

Ye et al. [54] applied strip theory based on blade element theory and the momentum theory to calculate the wind turbine performance and complex method which is one of the direct methods to solve the constrained optimization problems.

The panel theory for rotor systems was developed for helicopters and ship propellers by Foley in 1976 [55] and van Gent in 1975 [56]. The usage of this theory for wind turbines has begun by Sucie et al. in 1977 [57] and Preuss in 1980 [58] for example. The method discretizes the rotor blade and vortex sheet by a large number of surface elements with a singularity distribution on the surface or inside the blade volume.

Viterna [59] was the first person that suggested stall performance in HAWTs was critically important to understand and developed the prediction of peak power by considering blade aspect ratio as well as spanwise flow and pressure gradients in performance model because poor prediction of peak power,

included in aerodynamic loads, in high wind speed caused stall-controlled HAWTs to generate some errors and damages due to high stresses on turbine blades, which will shorten machine service life. In order to increase rotor performance without producing the large amount of lift coefficient in tip region of stall-controlled blade for control of peak power, Jackson [60] modified the blade optimization approach by introducing additional variables. On the other hand, Thumthae et al [61] investigated the relation between maximum performance in turbine blade without twist and angle of attack in several wind speeds and found that optimal angles of attack were obtained near the maximum lift point and that the angle sare larger as the wind speeds are higher. Then Garrad, Morgan and Hill [62] [63] showed the benefits of lower $C_{L,max}$ from the root region to the tip region for constant power stall characteristics in high winds. Robinson et al. [64] described the details of dynamic stall with vortex structure on HAWT blades due to the complex unsteadiness, separation and rotational influences.

Tangler [65] mentioned the lifting surface/prescribed wake performance prediction method (LSWT) to establish aerodynamics such as C_L, C_D and angle of attack and to model blade geometry and trailing vorticity distribution of the wake. It is argued that LSWT advances the ability to account for the induced effects of trailing vorticity and its influence on the angle of attack distribution, which elementary blade element/momentum theory is not.

Schreck et al. [66] [67] tested aerodynamic load enhancement due to rotational influences by obtaining aerodynamics forces and surface pressure distributions and believed that this helps better understand the fluid dynamic mechanisms responsible for aerodynamic load enhancement under rotational, three-dimensional conditions.

Filippone [68] presented his work of the design optimization of turbine blades and aerodynamic performance by inverse design method with viscous-

inviscid techniques, which concluded that $C_{L,max}$ accuracy, rotating effects and three-dimensional investigation needed to be verified for the reliability of the results.

Liu et al. [69] designed optimum model for wind turbine blades required targets power output in a specific wind site using the extended compact genetic algorithm (ECGA) which is faster and more accurate than the simple genetic algorithm such as direct method and complex method and found better aerodynamic performance.

Maalawi et al. [70] studied aerodynamic characteristics on HAWTs with direct method and an exact trigonometric function method in Glauerts approach which determined the optimum chord and twist distributions using analytical closed form equations, and concluded that the solutions were well convergent and unique due to the continuity of the angle of attack along blade span and it is more computationally efficient than other iterative procedures.

Chattot [71] proposed to maximize the torque under the constraint of the thrust force exerted by to rotor for a given tip speed ratio, taking into account viscous effect using helicoidal vortex model, Goldstein model [53]. It was concluded that the effect of viscosity correction is small on the optimum geometry but is significant on decrease in the efficiency of the turbine.

Maheri et al. [72] managed to reduce evaluation time in software simulation by decoupling the interaction between aerodynamics and structure which is so called bend-twist adaptive blades (BTABs). This can replace a finite element analysis (FEA) coupled with aerodynamics and structure (CAS) simulation in aerodynamic objective evaluation by a non FEA CAS simulation. This method gained potential benefits in order to improve the performance of wind turbines.

Habali et al. [73] discussed optimal aerodynamic efficiency by mixing sine different airfoils at the outer third of the span for small wind turbines and

found that turbine blades up to 5m long demonstrated good strength and aerodynamic characteristics.

Sicot et al [74] studied flow separation on an airfoil that related to the standard deviation of pressure in turbulent flow. The flow separation point showed some fluctuations whose length increased when the flow separation point moves towards the leading edge without the effect of Reynolds number or turbulence level on the Karman vortex shedding frequency. it is concluded that the results agreed with the study from the spectral analysis of aerodynamic loads. He also discovered that turbulence level has no significant effect on wind turbine torque and thrust since the distribution of the effect of turbulence level at lower angles of attack did not show large changes between 4% and 9% of turbulent levels [75]. These studies extended the stall mechanisms in rotation and turbulence effects on a horizontal axis wind turbine blade, which concluded that the stall phenomenon was less effect in lift increase because the pressure distribution in rotating blade did not influence the separation point position in turbulent flow [76].

3 Applications of Wind Turbine Technology

This report studied two wind turbine blades which are used for commercial wind turbines: Eppler387 and NACA63-215V. After reviews of both airfoil geometries in Section 3.2, the Eppler387 airfoils are re-designed in Section 3.4 by using a programme of direct surface curvature distribution blade design method developed by Hamakhan and Korakianitis [32] as discussed in section 2.2, chapter 2 and then a designed airfoil is analysed to assess aerodynamics by available data from National Renewable Energy Laboratory (NREL) [77] and from the report by a MEng student at Queen Mary in 2008. For the study of NACA63-215V, its aerodynamic calculations are also compared with available data obtained from Riso National Laboratory, Denmark [78] in Section 3.3. Also other existing airfoils in wind turbines, which are S814 and NAA63-221 are reviewed on aerodynamic calculation which have been done by a MSc student in Queen Mary and an internship student in 2009.

Section 3.1 reviews the characteristics that are important in analysis of aerodynamic calculation in Computational Fluid Dynamics (CFD) software, Gambit and Fluent. In section 3.2, the review of blade geometry describes in the form of curvature distribution, which is discussed in Section 2.2.1, Chapter 2. The predictions of the Eppler387 parameters from the turbine blade codes in a specific condition are shown by following the mechanism of velocity diagram mentioned in Section 2.1.4, Chapter 2. The detail of the rotational per minute calculations for Eppler 387 airfoil that has been studied is attached in Appendix 5.5.5.

3.1 Characteristics in CFD

As commercial computational fluid dynamics programmes have been developed, it is possible to predict airfoil performance in short time and re-design

for better performance based on those predictions. Fluent, a commercial fluid dynamics solver, allows wind turbine engineers to calculate the performance of those airfoils in a typical environment of a working wind turbine. Fluent uses non-linear solver and employs the Finite-Volume Method. The results of Fluent simulation will be compared with experimental data in this chapter.

It is important to note that a great role in aerodynamic calculation depends on some characteristics in CFD software, Gambit and Fluent for this study. The former includes grid scheme, grid quality and boundary layer while the latter viscous model, operating and boundary conditions and dimensionless wall distance. In addition to them, curvature distribution for geometry analysis should be taken into account. These factors help understand the fluid mechanism over an airfoil, control the domain and reduce the time consuming in the calculation.

3.1.1 Grid

The mesh construction is needed for an accurate analysis of fluid mechanics along an airfoil. The computational result and calculation period heavily depend on mesh characteristics. The mesh quality is judged by the quantity, position and type of mesh which is determined from the shape of the object face. Firstly the number of nodes should be positioned along an airfoil to draw shape as close as the original geometry. This is because the node density could change the original shape in especially non-straight lines. This affects the total result of a study. It can be prevented from by considering nodes grading. Secondary the mesh type and element are specified as map for creation of a regular, structured grid of quadrilateral or quadrilateral and triangle mesh elements in this study. For the case of turbulent flow, the feature of grid can be classified by no dimensional wall distance (y+) which is discussed later in this chapter.

3.1.2 Boundary layer and Reynolds number

Boundary layer is a thin layer of air and appears on the surface of objects in viscous flow because the fluid seems to stick to the surface. The boundary layer effect depends on the flow pattern which is related to the Reynolds number. At low Reynolds numbers, it is low skin friction, shear stress which describes laminar flow. The instabilities of the flow develop and the flow transition changes into turbulent motion as the fluid is sheared across the surface of the object. This causes to thicken the boundary layer with higher Reynolds numbers. As shown below, Reynolds number is a function of fluid velocity.

$$Re = \frac{\rho V C}{\mu} \tag{37}$$

Where ρ is the fluid density, V is the mean velocity of the fluid, C is a chord length and μ is the dynamic viscosity of the fluid.

Figure 29 shows the relation between Reynolds number and fluid pattern. In this study, Reynolds numbers were used 1×10^5 for Eppler387 and 1.1×10^6 for NACA63-215V which are turbulent flow for the both case as seen from the figure. However Eppler 387 operates in inviscid flow which has no viscosity and no drag will be produced. Therefore there is no boundary layer over the airfoil of Eppler387.

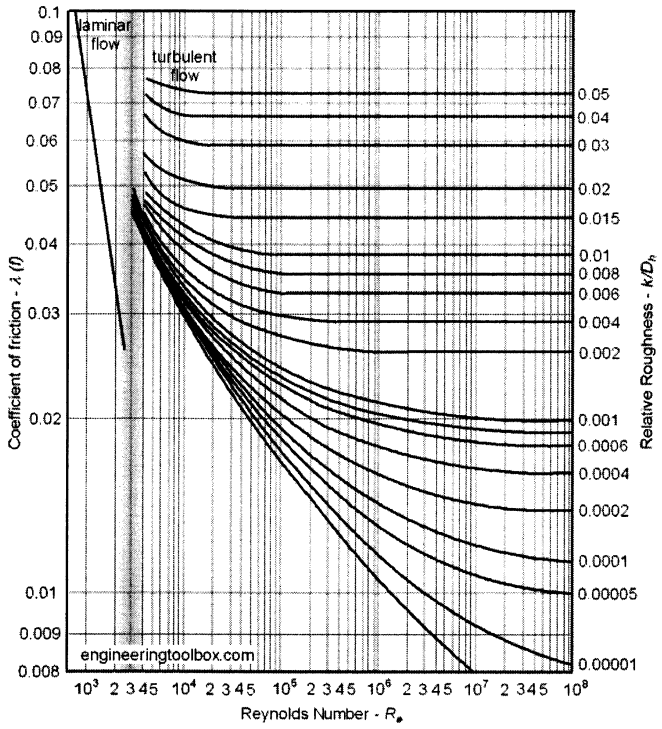

Figure 29: Moody diagram for analysis of fluid pattern and Reynolds number [79]

3.1.3 Mesh quality

Examination of mesh is to check the quality of mesh in a domain. Good mesh means good quality and leads good result and aerodynamic calculation in much short period of time. In this study, EquiAngle Skew was used to check skewness of the mesh, which is defined as

$$Q_{EAS} = max\left(\frac{\theta_{max} - \theta_{eq}}{180 - \theta_{eq}}, \frac{\theta_{eq} - \theta_{min}}{\theta_{eq}}\right) \tag{38}$$

Where θ_{max} and θ_{min} are the maximum and minimum angles in degree between the edges of the element and θ_{eq} is the characteristic angle corresponding to an equilateral cell of similar form. When quadrilateral mesh is used, then θ_{eq} is 90. When triangle mesh is used, then θ_{eq} is 60. It is defined that EquiAngle Skew is between 0 and 1 which describes a completely

degenerate element. Mesh quality shows excellent by 0.25 and good by 0.5.

3.1.4 Viscous model

Viscous models used in this study were inviscid for Eppler 387 and k-omega SST turbulence for NACA63-215V.

The $k-\omega$ SST turbulence model is based on the standard k-omega model which is a model of transport equations for the turbulent kinetic energy, k, and its specific dissipation rate, ω, and is taken account for the shear stress transport in turbulence (SST). The $k-\omega$ SST is considered more accurate and reliable for a wide range of flow such as airfoils and transonic shock waves by effectively combining the formulation of the $k-\omega$ model in the near-wall region with the free-stream independence of the k-epsilon model in the far field.

3.1.5 Boundary condition and operating condition

The operating condition of wind turbine blade is considered at sea level. Table 4 shows the parameters in the condition for each case of the blades.

3.1.6 Dimensionless wall distance ($y+$)

$y+$ is a mesh-dependent dimensionless distance that qualifies to what degree the wall layer is resolved because turbulent flows are significantly affected by the presence of walls. In other words, successful prediction of turbulent flows is determined by accurate presentation of the flow in the near-wall region. The value of $y+$ in the wall-adjacent cells dictates how fine a mesh is for a particular flow or how wall shear stress is calculated. $y+$ of the wall-adjacent cells is better small to the order of $y+ = 1$ when the transitional flows option is enabled in the viscous model. In the case of near-wall modelling, the viscous

Table 4: Parameters in the operating conditions

Property	Eppler387	NACA63-215V
Level	Sea level	Sea level
Temperature ($degree$)	15	15
Density (kg/m^3)	1.225	1.225
Viscosity ($kg/m.s$)	1.7894E-05	1.7894E-05
Atmospheric pressure (Pa)	102325	102325
Reynolds number	1.0×10^5	1.1×10^6
Air velocity (m/s)	13	16.07
Turbulent intensity (%)	0	3.13
Turbulent viscosity ratio	0	1

sublayer is $y+ \leq 5$, $5 < y+ < 30$ for buffer region and $30 < y+$ for fully turbulent region. Solutions with $y+$ values in the buffer region are generally less accurate than the others. For the case in non-transitional flows option which is wall functions, $30 < y+ < 300$ is called log-law layer in which each wall adjacent cells centroid is located and $y+ = 30$ is most desirable. In this study, it is $k-\omega$ SST viscous model with near-wall modelling.

$$y+ = \frac{\rho\, u_\tau\, y_p}{\mu} \tag{39}$$

Where ρ is the fluid density, u_τ is the friction velocity, $\sqrt{\frac{\tau_\omega}{\rho_\omega}}$, y_p is the distance from point P to the wall and μ is the fluid viscosity at point P.

Accurate result is explained when a turbulence model is coupled with a appropriate near-wall treatment approach. Salim et al [80] describes that accuracy increases in the sufficient resolution of the near-wall mesh for the $k-\omega$ model which is designed to be applied throughout the boundary layer. In other words, for the case of $k-\omega$ model, the smaller cell sizes the more accurate result. This is because more details is captured during computation.

3.1.7 Curvature distribution

Geometry of original airfoil blade can be analysed by computing curvature, $C = \frac{1}{r}$, from coordinates. This is the same principle as a circle from 3 points in 2D. The technique for determining the characteristics of a circle given three points on a plane is described in Figure 30.

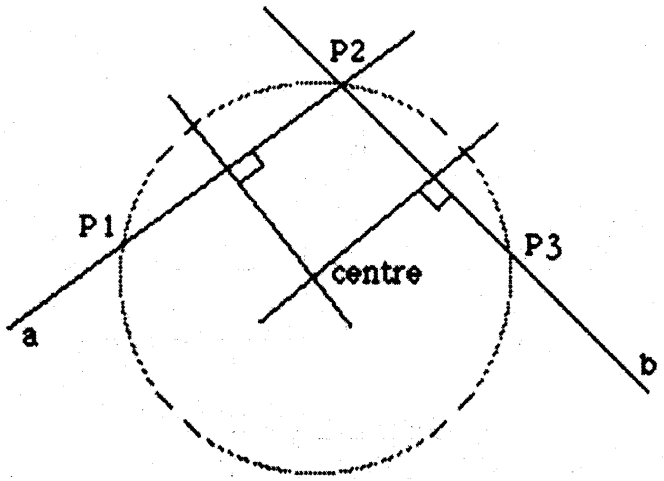

Figure 30: A circle from 3 points in 2D [81]

The equation of two lines, a and b is

$$y_a = m_a\,(x\,-\,x_1)\,+\,y_1\,or\,y_b = m_b\,(x\,-\,x_2)\,+\,y_2 \tag{40}$$

Where m is the slope of the line given by

$$m_a = \frac{y_2 - y_1}{x_2 - x_1}\,and\,m_b = \frac{y_3 - y_2}{x_3 - x_2} \tag{41}$$

The slope of a line in perpendicular to the line of P_1P_2 and P_2P_3 is $-\frac{1}{m}$. With this, the intersection that passes through the centre is

$$x = \frac{m_a\,m_b\,(y_3 - y_1) - m_b\,(x_1 + x_2) + m_a\,(x_2 + x_3)}{2\,(m_a - m_b)} \tag{42}$$

The y value of the centre can be calculated by substituting the x value. Hence the radius of the circle is obtained as the coordinates of the centre of the circle is $(x_c\,,\,y_c)$.

$$r = \sqrt{(x_c - x_1)^2 + (y_c - y_1)^2} \tag{43}$$

The curvature, $C = \frac{1}{r}$, is computed.

3.2 Blade Geometry

3.2.1 Eppler387

Eppler387 airfoil is used in a wide range of wind turbine application and vehicle application such as military and civil in low Reynolds number with emphasis on providing better performance. Reynolds numbers below 500,000 are identified as being in this classification. Eppler387 is relatively thin airfoil as shown in Figure 31.

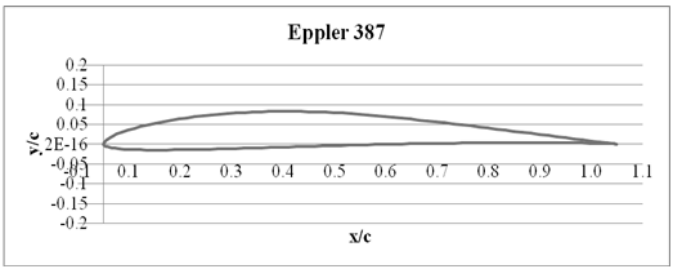

Figure 31: Eppler 387 geometry, data from [82]

Figure 32 shows the curvature of the airfoil, the log values of R. The curvature describes the smoothness on blade surface which causes flow separation at the point of discontinuity over the blade and leads to poor performance of wind turbine. This is discussed in Section 2.2.1, Chapter 2. R is a radius of a circle made from 3 points on and along the blade of the value of 1 to -1. It can be seen from the figure that there are some spikes in the both sides of

the airfoil and especially the curve making the leading edge has a big break. The tail part of the trailing edge on both sides, suction and pressure sides shows also spikes between 0.7 and 1 in x/c distance from the leading edge. It is a visible peak around 0.3 in x/c from the leading edge on the pressure side of Eppler387. Those spikes tell discontinuities at the points due to lack of continuous curvature and the slope of the curvature along the blade. And the discontinuity will be disturbing the velocity and pressure of the flow around the airfoil.

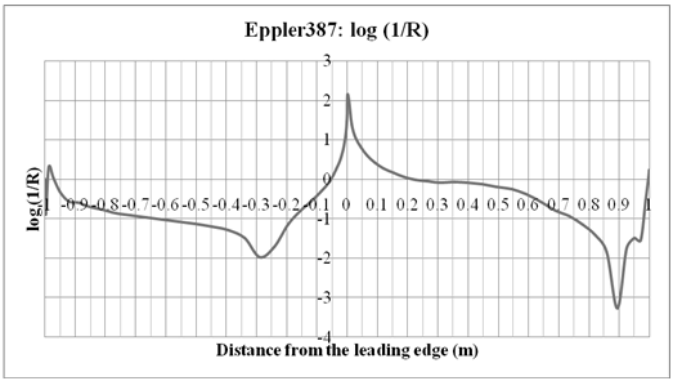

Figure 32: Curvature (C) of Eppler 387. Data from [82]

Table 5 shows property parameters at three section, hub, mean and tip section of the blade in the condition of working wind turbine. The rotor diameter is 1.75m [82] and 13m/s ($Re = 1 \times 10^5$) for the operating wind speeds. It can be seen from the tables that the power of the Eppler blade calculated using the velocity diagram are 1.75kW. The TSR of Eppler387 at 13m/s is 6.46 which is an ideal figure for three-blade as discussed in Chapter 2.

Table 5: Power calculation of Eppler387 using velocity diagram

	Radius (r)	Mass flow rate ($\dot{m}$)	Tangential velocity at outlet ($C_{u,2}$)	Power (W)
Hub	0.292	2.3	3.1	360
Mean	0.584	12.8	1.5	1080
Tip	0.875	21.2	1.0	1745

3.2.2 NACA63-215V

NACA63-215V is one of the NACA wing section families and is used on wind turbines. The three digits indicate the design lift coefficient for the first digit and the thickness for the last 2 digits. The letter V refers to VELUX measurements in wind tunnel test. Hence the experimental data of NACA63-215V is measured in the VELUX wind tunnel, which has an open test section.

The study focuses on the analysis of the NACA63-215V aerodynamic calculation by using commercial software, Fluent which is a non-linear solver and employs the Finite-Volume Method. The results obtained from the Fluent simulation are compared to the data from numerical simulations with the 2D incompressible Navier-Stokes solver, EllipSys2D, with the data from the XFOIL code which is a linear equation solver based on a panel method combined with a viscous boundary layer formulation and experimental test. The numerical data and experimental data are found from Riso National Laboratory, Denmark [78].

Figure 33 and Figure 34 show the geometry and the blade surface distribution of the airfoil. It can be seen from the curvature distribution that NACA63-215V has problems around the leading edge, between 0.7 and 0.8 and around trailing edge on the both sides of the blade.

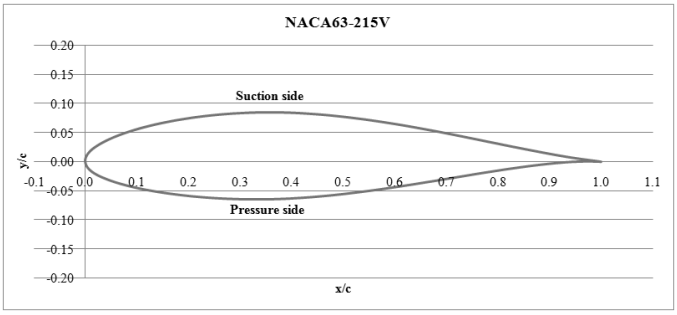

Figure 33: NACA63-215V geometry, data from [78]

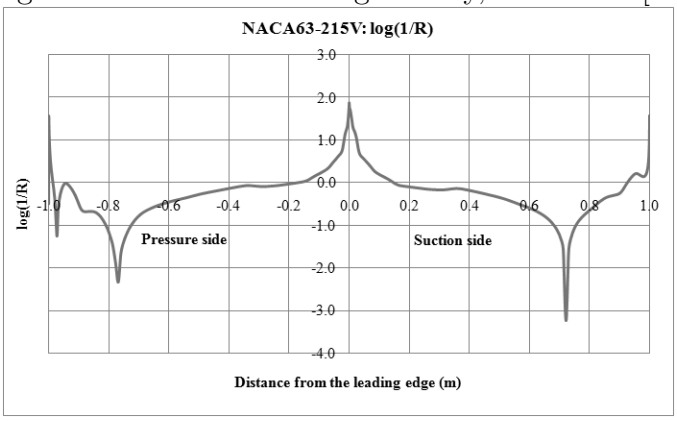

Figure 34: Curvature of NACA63-215V, data from [78]

3.3 Aerodynamic Calculations

This chapter discusses four wind turbine blades: Eppler387, NACA63-215V, S814 and NACA62-221. They are different shapes and hence corresponding aerodynamics are different. Figure 35 shows the geometries of the airfoils.

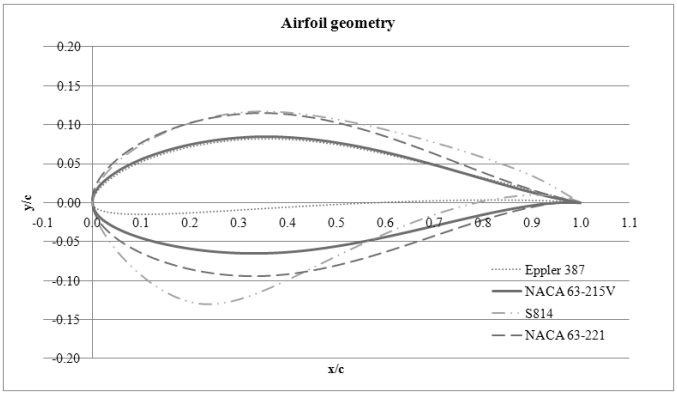

Figure 35: Comparison of airfoil geometry, data from [82] [78]

3.3.1 Eppler387

Rahman [83] studied the Eppler387 airfoil geometry which might cause a noise production in wind turbines in the condition of Reynolds number 1×10^5 which produces a flow speed of 13 m/s. This study was organised with inviscid flow and without any incident of the flow. He discovered that the discontinuities of the surface of Eppler387 in the curvature profile agreed to the pressure fluctuations at the same points due to flow disturbance that the pressure of sound signal occurred at the same position as that of curvature and pressure coefficient. He hence concluded that the pressure fluctuations cause sound generation. This is shown in figure 6.6, figure 6.8 and figure 6.12 in [83].

3.3.2 NACA63-215V

The NACA63-215V airfoil was created in a C-mesh with quadrilateral mesh element of 7500 mesh faces on each side of the airfoil. The mesh quality of the whole domain was high, of which the pressure side of the airfoil remained by 0.19 of skewness whose figure is still a good result.

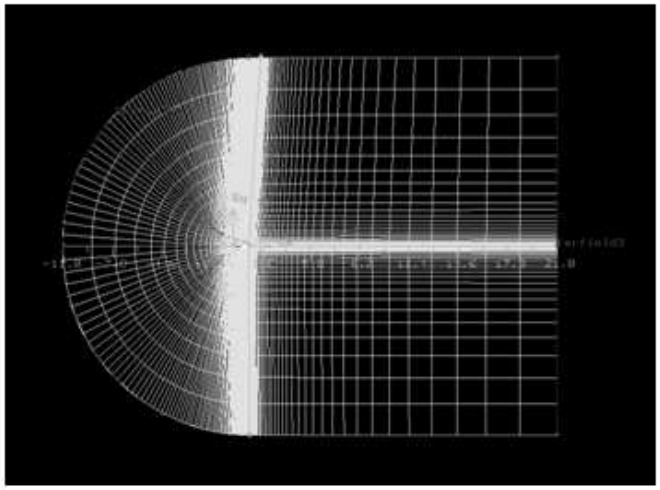

Figure 36: Full view of mesh over NACA63-215V

In this study of NACA63-215V, the flow is turbulent and in viscous model.

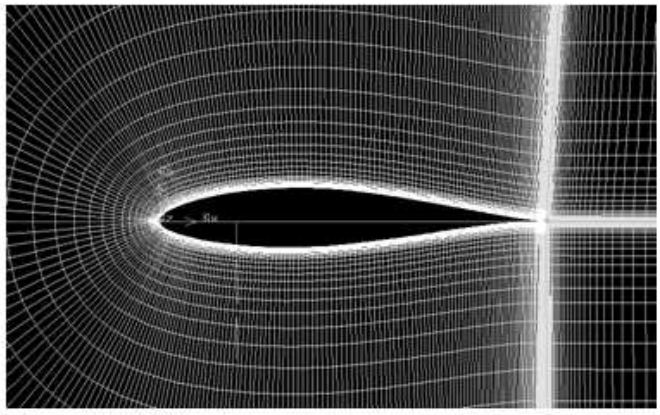

Figure 37: Mesh along NACA63-215V

The boundary layer was created unlike the previous case of Eppler387. Table 6 shows the details of the boundary layer over the NACA63-215V in Gambit.

The aerodynamic calculations for three cases were run and compared in the range of angle of attack between 5.741 and 15.578 degrees. Mesh 3 and Mesh 5 have the different characteristics of mesh nodes and boundary layers hence individual mesh quality as shown in Table 6. The Case (a) and (b) were different in the boundary layer feature to see corresponding wall $y+$ by change in first row and the number of rows of the boundary layer. Case (b) was produced finer mesh in boundary layer than Case (a).

The feature of the mesh was produced and might differ on each of the faces over the airfoil: suction side (upper face) and pressure side (lower face), due to non-symmetrical shape. In the table below, suction side represents SS and pressure side PS.

Table 6: Mesh and boundary layer characteristics on NACA63-215V

	Mesh 3(a)	Mesh 3(b)	Mesh 5(a)	Mesh 5(b)
Nodes (each side of airfoil)	150	150	200	200
Mesh faces (along airfoil)	7,500	10,500	14,000	16,000
Node grading	Bell Shaped (BS)	BS	BS	BS
Node ratio (SS, PS)	0.7, 6.9	0.7, 6.9	0.7, 0.7	0.7, 0.7
Mesh element	Quadrilateral (Q)	Q	Q	Q
Mesh type	Map	Map	Map	Map
Mesh quality (EquiAngle Skew, > 0.1)	5.35%	5.19%	4.51%	5.71%
First row	1.5E-04	1.0E-04	1.0E-04	5.0E-05
Growth factor	1.2	1.2	1.2	1.2
Number of rows	20	30	20	40

It can be seen from the figures of wall $y+$, Figure 38 that Case (b) of Mesh 3 and Mesh 5 in the range of angle of attacks have $y+$ characteristics laying in the viscous sublayer, between 1 and 5 which is desirable for near-wall modelling. The mesh configurations hence tend to increase more accuracy of prediction of turbulent flows. The $y+$ values of Mesh 3(a) and Mesh 5(a) around the leading edge and trailing edge however are almost the same due to the lack of clustered mesh near wall region and expected less precision in aerodynamic calculations since much of part of suction side between the leading edge and the main body, in smaller angle of attacks, is stepped in buffer region.

On comparison of these cases to the data of experiment in lift and drag

coefficients in Figure 39, the results obtained from Fluent calculations agrees with experimental data in regard of drag coefficient at lower angle of attacks, up to 12 degrees. It can be said that the Fluent solution in turbulent flow achieves good agreement over the angle of attacks As angle of attack increases, the results of Mesh 3(a) and Mesh 5 (a) are closer to the experimental data than Mesh 5(b) which is expected to show more accurate prediction of flow over airfoil. However the results of Mesh 3(a) and Mesh 5(a) could be less accurate as their $wall - y+$ figures are out of desirable region at especially leading edge.

The lift and drag coefficients of Mesh 5(a) and 5(b) are compared to the data from Riso National Laboratory, Denmark [78] in Figure 40 with the consideration of accuracy of flow behaviour prediction by the wall $y+$ results and in spite of output of slightly larger gap to experimental data than the other cases . The results, shown in the figures below, indicate very good agreement with experimental data despite the increase in difference at higher angle of attacks where stall starts appearing. Here the difference between the results from EllipSys2D and Fluent has to be marked that the both calculations are run in turbulent flow but EllipSys2D shows less sensitive to the conditions such as background turbulence level and roughness of the airfoil surface. It is reported in [78] that EllipSys2D code makes bigger discrepancies in the airfoil that is thick and has a sharp leading edge suction peak region and a low pressure gradient on the suction side of the airfoil. In fact, the thickness and the leading edge curvature of NACA63-215V is 15% and 37 at maximum respectively while those of NACA63-211 and S814 of which aerodynamic calculations are obtained by [33] and [35] are 21% and 23.2, and 24% and 21.8 respectively.

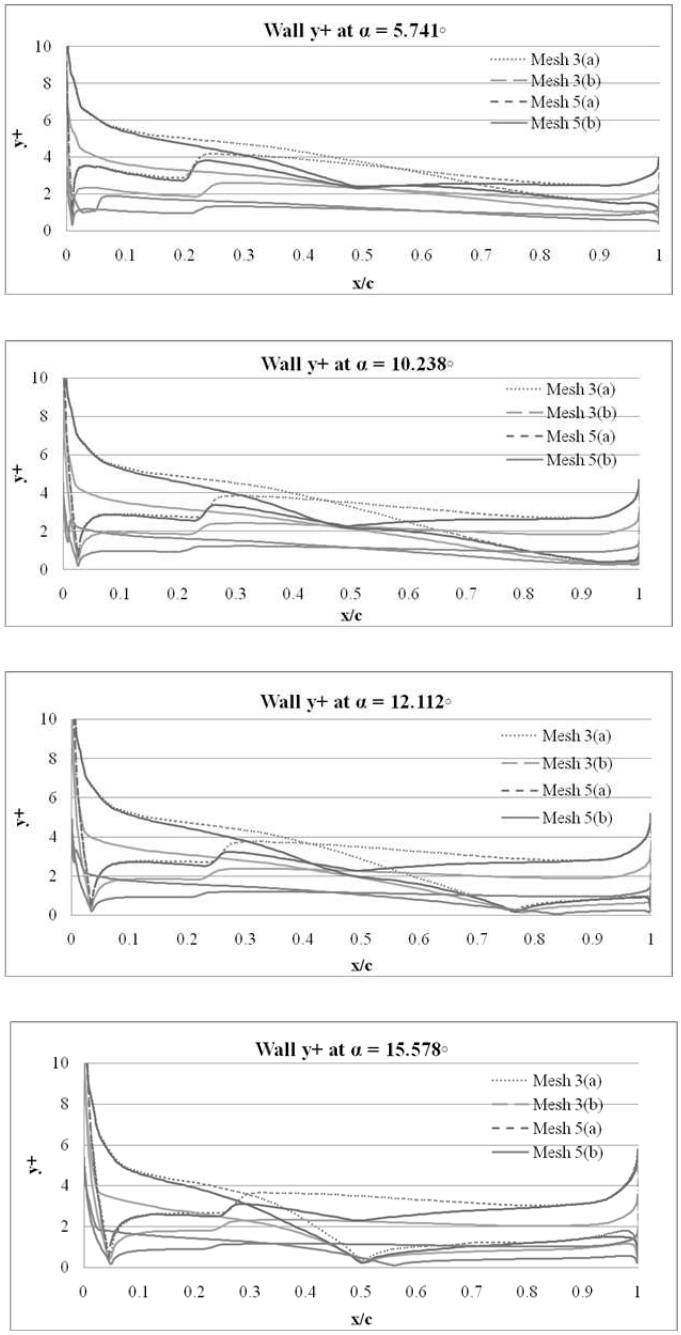

Figure 38: Wall y+ distribution (NACA63-215V)

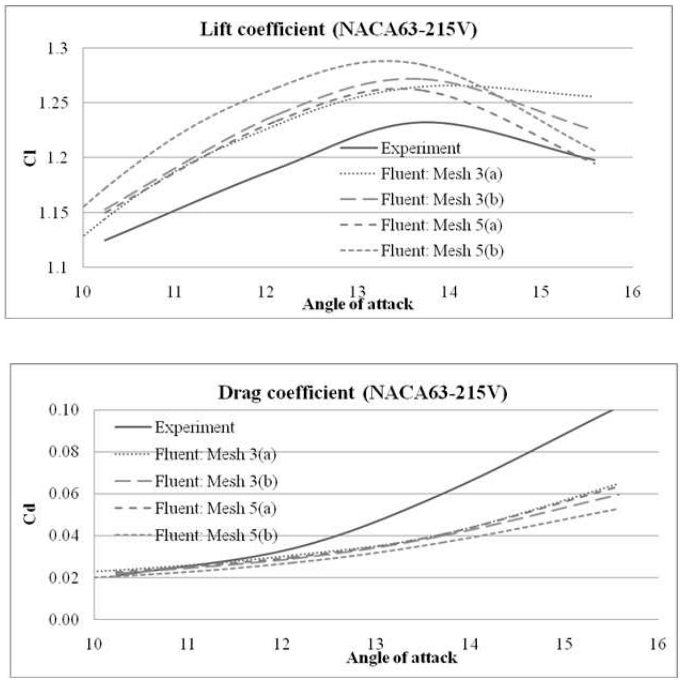

Figure 39: Lift and drag coefficient in various mesh cases (NACA63-215V)

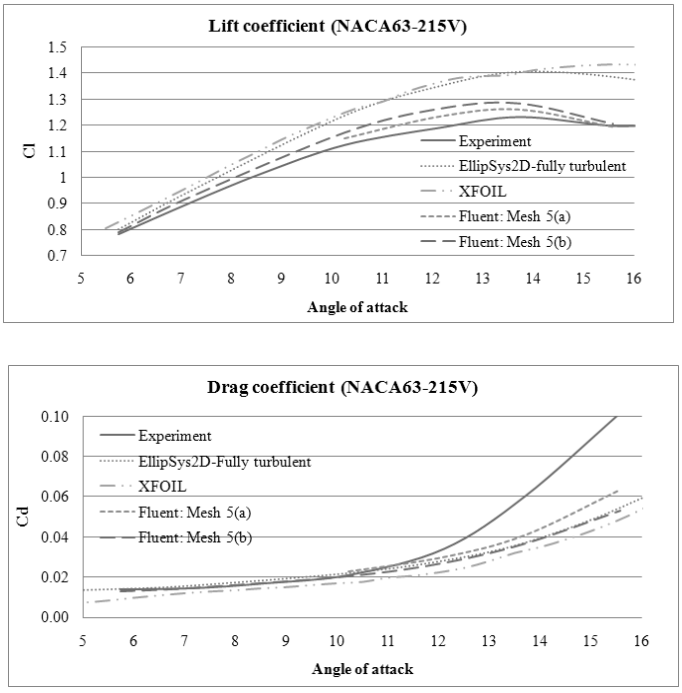

Figure 40: Lift and drag coefficient distributions (NACA63-215V)

Also the agreement between Fluent and the others can be seen on pressure coefficient at angle of attacks as shown in Figure 41. The spikes at the leading edge on pressure side can be seen in XFOIL code in the all cases while EllipSys2D draws no fluctuations. The Fluent results on the other hand are very similar to ones from EllipSys2D but obtained small changes in pressure coefficient on leading edge at the lower angle of attacks of 5.741 degrees to 10.238 degrees. The spikes at the leading edge on pressure coefficient are seen over the same positions in the NACE63-215V curvature, Figure 34, which concludes that the points where the surface of the airfoil has a high curvature are where the pressure of the flow over the airfoil is disturbed. Comparing these three methods with experiment on pressure coefficient in the range of angle of attacks, the agreements with experimental data decrease at higher angle of attacks.

3.3.3 S814

The S814 airfoil has been designed at National Renewable Energy Laboratory (NREL) in the United States. It is a 24% thick wind turbine blade while NACA63-215V is 15% and NACA63-221 which is discussed in the next section is 21%.

The round shape of leading edge such as S814 has an issue of surface roughness on the leading edge caused by insects and rain at the higher lift coefficient. Somers [84] reported that the big issue on the S814 airfoil is the roughness of the airfoil surface which affects largely the lift coefficient. The maximum lift coefficient decreases 1.51 by 0.05 for the case of Reynolds number of 1.5×10^6 and this effect is thought to be severe than one caused by the usual manufacturing irregularities or deterioration in services.

The study of S814 was done in the similar process to the previous model, NACA63-215V, by Vlieghe [35] for angle of attack ranging from 4 to 12 de-

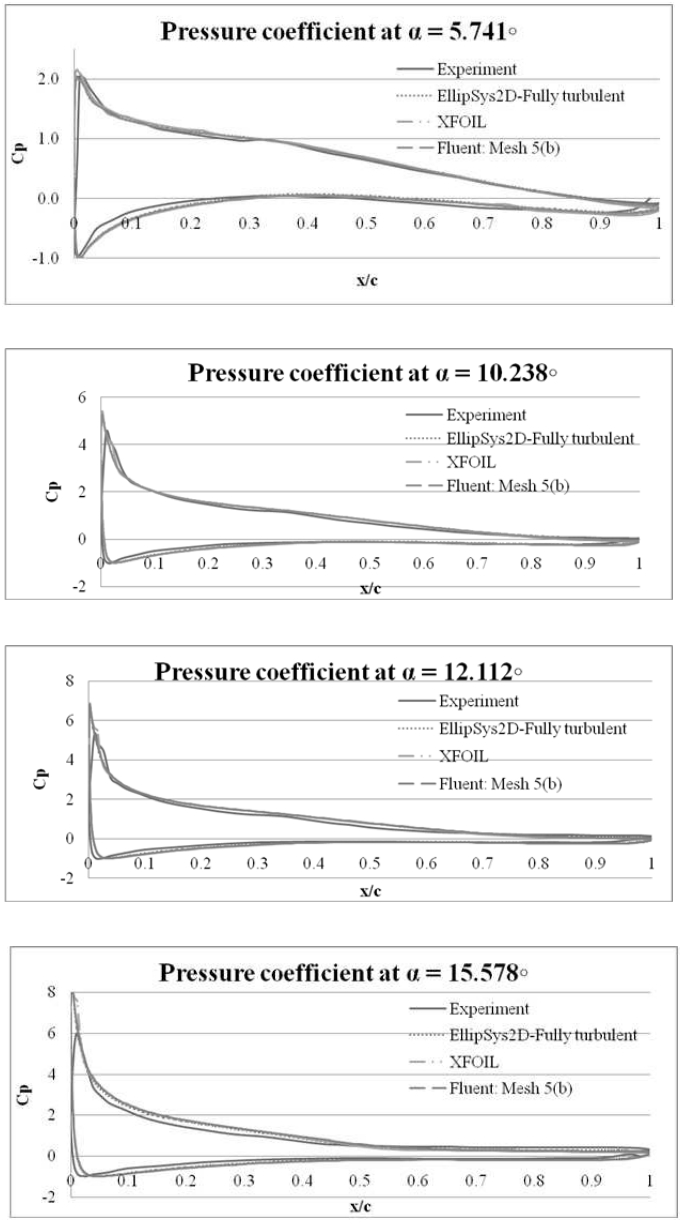

Figure 41: Pressure coefficient distributions (NACA63-215V)

grees, with comparison to the data from Riso National Laboratory, Denmark [78]. Reynolds number on this study is 1.0×10^6, equal to 14.6 m/s of free stream of the flow. The turbulent intensity is 2.85% and a fully turbulent flow solution was used in Fluent, where $k - \omega$ SST model was used for the turbulent viscosity. The curvature distribution showed discontinuous curve at around 0.25 on the both sides, 0.5 on the suction side and between 0.9

and 0.95 on the pressure side. However those spikes were not seen in the pressure distribution over the S814 airfoil. Vlieghe [35] concluded that the results obtained from Fluent calculations agreed very well with experimental data and numerical data in regard to lift, drag and pressure coefficients.

3.3.4 NACA63-221

The NACA63-221 airfoil which is thicker and curvy shape over the leading edge as mentioned earlier was studied by Rahman [83]. Reynolds number for this case is $Re = 3.0 \times 10^6$ and win speed is 10 m/s. In the Fluent calculation, $k - \omega$ SST was used for turbulent viscosity. He found that pressure distribution on the suction side of the airfoil was disturbed as the angle of attack increased but there were no flow separations at lower angle of attacks. The pressure disturbance on the suction side was removed by designing the airfoil surface curvature to smooth using the programme of direct surface curvature distribution blade design method developed by Hamakhan and Korakianitis [32]. The flow separation instead occurred at lower angle of attacks and fully developed at higher ones. He concluded that smooth surface-curvature is necessary to minimise flow separation.

3.4 Potential for improvement on Eppler387

The Eppler387 airfoils in section 3.4 are re-designed by using a programme of direct surface curvature distribution blade design method developed by Hamakhan and Korakianitis [32] in order to maximise the aerodynamic efficiency. The parameters used in the programme are shown in Appendix 5.6. The Eppler387 airfoil problems in surface curvature discontinuities were shown in the surface pressure distribution in [83].

Figure 42 show the difference in geometry of Eppler387 from a similar geometry Eppler387 created using direct curvature blade design method. To

keep the blade chord as x = [0, 1], the leading edge is a slender shape and the foremost point on the designed Eppler387 is at (x, y) = (0, 0). The trailing edge on the other hand is designed slightly thicker due to the effect of the trailing edge circle in the design programme and the aft point is at (x, y) = (0, 0.000128).

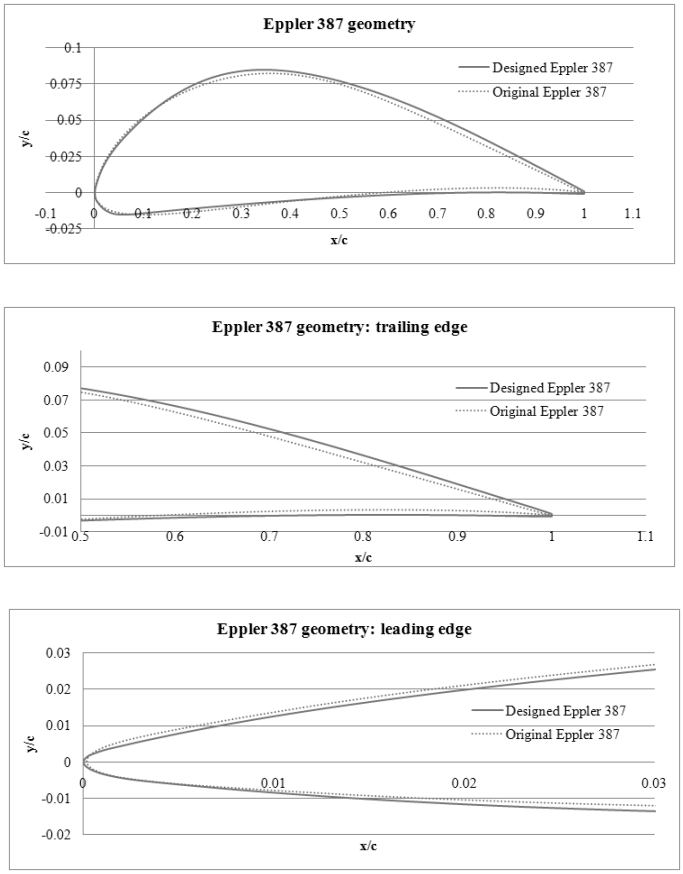

Figure 42: Comparison of blade geometry of Epper387

It can be seen from Figure 43 and Figure 44 showing the surface curvature of the airfoils that the curvature drawn in the direct blade design programme is smooth without edges or spikes along the main body but has very sharp turns around the leading and trailing edges. This is shown in the curvature calculated from the airfoil coordinates. In addition to those discontinuities of surface, some fluctuations towards the leading edge from 0.3 on the pressure side and at 0.5 on the suction side are seen. The sharp peak at 0.3 on the

pressure side is thought at the point of P_{pm} where is the junction between the trailing edge pressure side and the main Bezier pressure side as shown in section 2.2.1, chapter 2. It was reported by [33] and [35] that the blade design of the pressure side, especially at P_{pm}, failed to find an airfoil shape, hence could not obtain a smooth curvature. Those effects are shown in Figure 5.8 and 5.9 in [33], and Figure 5.2 (a) and (b) in [35].

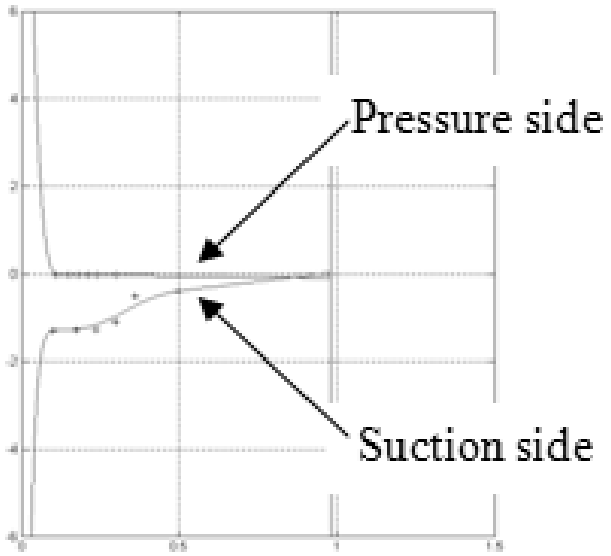

Figure 43: Curvature distribution of designed Eppler 387 in blade design programme

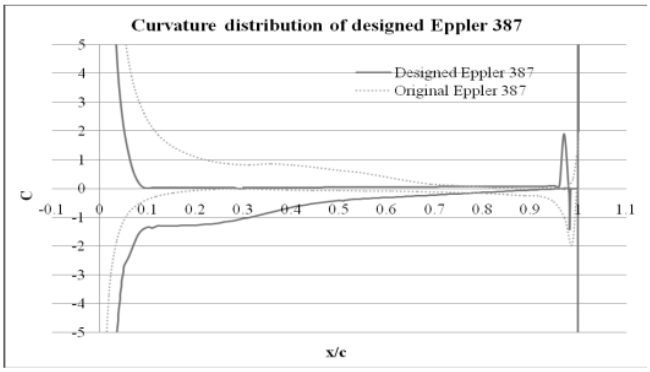

Figure 44: Curvature distribution of designed Eppler 387 from coordinates

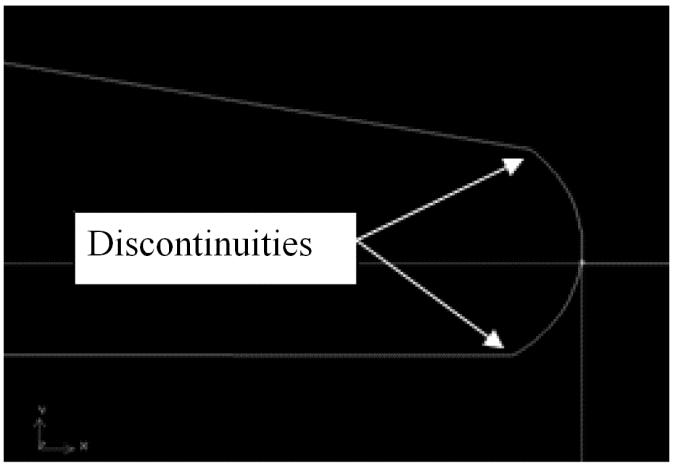

Figure 45: Trailing edge of designed Eppler387

It can be seen from the shape of the trailing edge of designed Eppler387 drawn by Gambit in Figure 45 that the curvature of the part is discontinuous with the slopes connected to the suction and pressure sides of the main body to the trailing edge circle. The discontinuities are clearly seen in the curvature diagram that the trailing edge on the both suction and pressure sides creates edges and draws sharp curvatures. Hence the equation of the trailing edge region which was discussed in Section 2.2.1 in Chapter 2 does not have equal second and third derivatives with the trailing edge circle at the points P_{s2} and P_{p2}, $x = x(P_{s2})$ and $x = x(P_{p2})$. This discontinuity will be able to be smoothed by decrease in the diameter of the trailing edge circle or/and change in angle of slope between P_{s2} and P_{sm}, bmr in the design programme. This causes a problem in grid design in Gambit that Gambit cannot accept the geometry and automatically modifies the trailing edge shape unless the edges are split at the points.

Computational mesh was done in Fluents mesh tool Gambit. The mesh consists of 30,100 quadrilateral and triangular mesh faces, of which 330 is on the airfoil. The mesh quality can be discussed by the examination of characteristics of mesh such as skewness. For this study, EquiAngle Skew was tested between 0 and 0.5 whose range is considered as good mesh in quality

and was 165 elements which are equal to 0.55% of the whole mesh beyond the range. It is discovered that those meshes are along the trailing edge circle. Table 7 is the summary of mesh characteristic used in Gambit and Figure 46 shows mesh outlook and quantity over the blade in the C-mesh domain.

Table 7: Mesh characteristics on designed Eppler387

Nodes along airfoil	160 (suction and pressure sides)
Node grading and ratio	Successive, 0.71(suction side), Successive, 0.755 (pressure side)
Mesh element	Quadrilateral and Triangular
Mesh type	Map
Mesh quality (EquiAngle Skew, > 0.5)	165 elements (0.55%)

Reynolds number for the simulations is $Re = 1 \times 10^5$ in turbulent flow and Mach number is 0.038 (subsonic) with 13 m/s of the wind velocity. A inviscid flow model was used in Fluent.

It can be seen from the pressure distribution over the designed airfoil in Figure 47 that small spikes are discovered around the leading edge and on the pressure side trailing edge. These fluctuations agree with the problems on the curvature distribution of designed Eppler blade. Similarly the main body of the airfoil did not illustrate spikes or dips as the curvature distribution has drawn smooth line. Hence it can be stated that the total pressure is significantly constant unlike the study of original Eppler387 by Rahman [83] despite the production of visible dip and fluctuation at leading and trailing edges. He concluded that original Eppler387 created a boundary layer near to the wall due to viscosity.

Comparing to the data predicted by the Eppler airfoil design and analysis code, PROFIL00, which is a code combined with a conformal-mapping

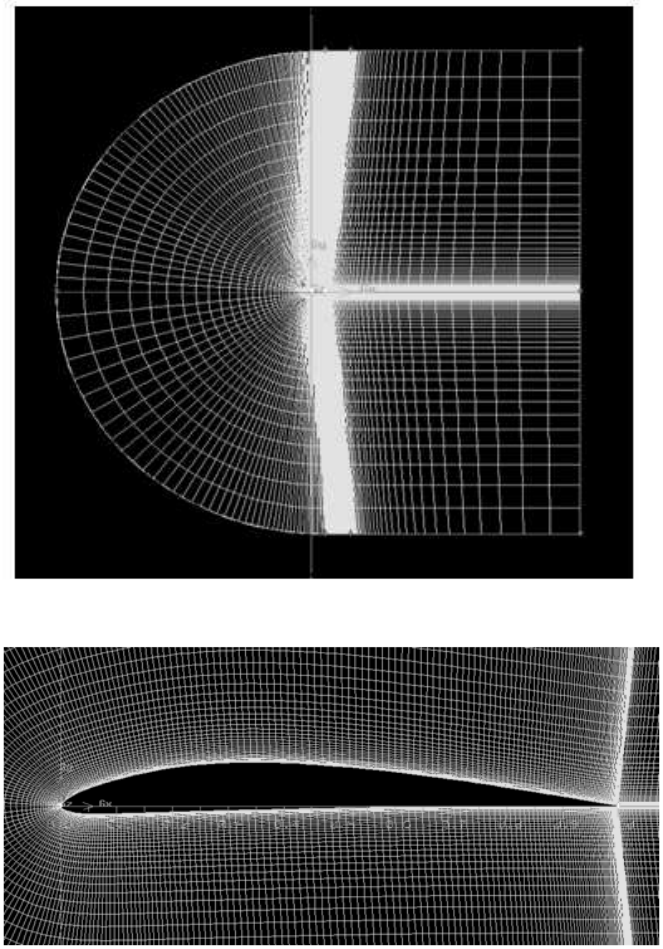

Figure 46: Mesh around designed Eppler387

method, a panel method and an integral boundary-layer method, from NREL [77], the designed Eppler387 has a problem that the surface curvature distribution at LE is noticeable on C_p graph at both angle of attack. The dip decreases in higher angle of attacks on pressure side while it increases in lower angle of attacks on suction side shown in Figure 48.

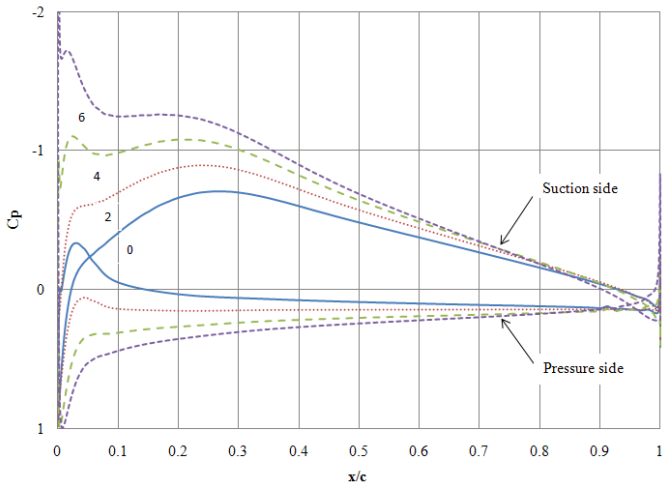

Figure 47: Pressure distribution of designed Eppler387, a = 0 to 6

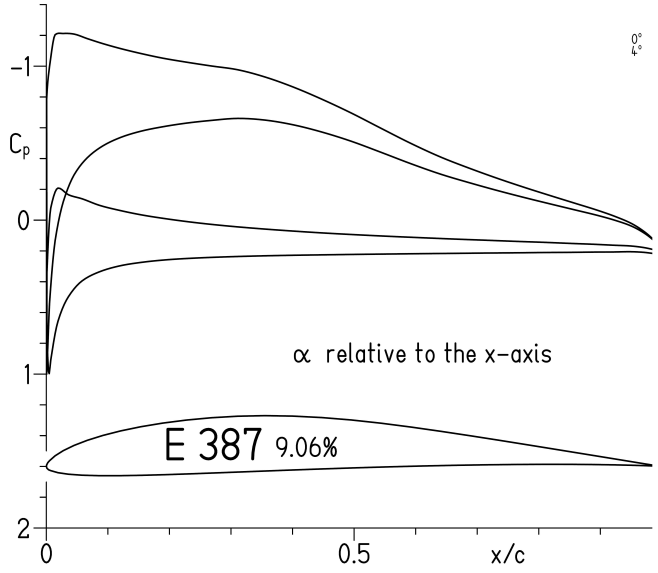

Figure 48: Pressure distributions for Eppler387 airfoils at a = 0 degree (inside) and 4 degrees (outside) [77]

The lift and drag coefficients from Fluent on the designed Eppler387 are compared at various angles of attack between 0 and 6 degrees with ones on original blade. The figures in Figure 49 show that the results are much lower than theoretical values which are 7.81E-03 for lift coefficient and 9.727E-04 for drag coefficient at zero angle of attack [83]. It can also be said that the lift is not sensitive to small changes in surface pressure as the designed

Eppler387 has stable lift coefficient over the angle of attacks and the lift-curve slope sustains the same value as one of the original Eppler387 obtained from XFOIL. This indicates that the thicker blade does not affect surface condition to keep the lift coefficient predicted for the original Eppler387. The results could converge up to 6.5 degree of angle of attack.

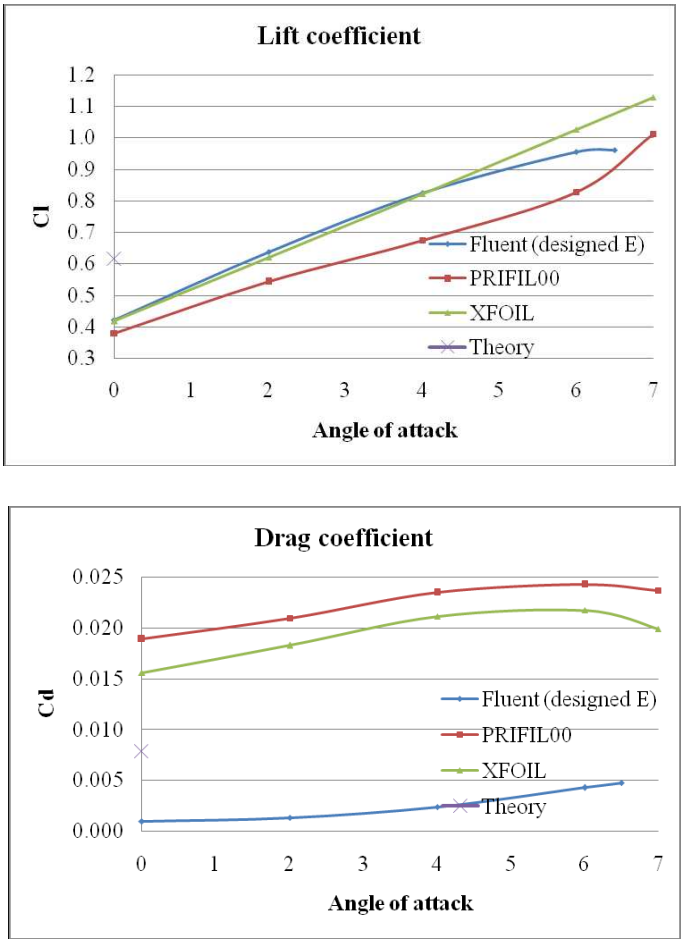

Figure 49: Lift and drag coefficients of designed Eppler387 with Fluent

4 Conclusions

The study of rotor blade aerodynamic performances of wind turbine has been presented in this thesis. This study was focused on aerodynamic effects changed by blade surface distribution as well as grid solution along the airfoil. The details of numerical calculation from Fluent were described to help predict accurate blade performance for comparison and discussion with available data.

The direct surface curvature distribution blade design method for two-dimensional airfoil sections for wind turbine rotors have been discussed with the attentions to Euler equation, velocity diagram and the factors which affect wind turbine performance and applied to design a blade geometry close to an existing wind turbine blade, Eppler387, in order to argue that the blade surface drawn by direct surface curvature distribution blade design method contributes aerodynamic efficiency.

The pressure distribution of NACA63-215V did not show the spikes that was seen in the surface curvature distribution. The aerodynamic characteristics agreed well with experimental data at lower angles of attack in this study. It can be said therefore that the discontinuities around between 0.7 and 0.8 in x/c on both sides of the airfoil are so small that the blade performance cannot be affected to decrease the aerodynamic characteristics by the accurate control on boundary layer.

Eppler 387 has been designed using direct surface curvature distribution blade design method. The surface distribution of the designed Eppler matched the curve of the pressure coefficients. Despite of geometrical issue at some point over the new airfoil, it was successful in reduction of drag effect and in keep lift coefficient. From the experimental point of view, there always happened some issue on the leading edge pressure side, which was also mentioned by [33] and [35]. The LEPS curvature turned away from an expected line

or shape at the last point of Bezier curve, which might be caused by the connection between the coordinates of the construction line at LEPS and of the main Bezier pressure side. It was seen that the trailing edge shape was not ideal in terms of continuity of the connection between a circle and the trailing edge pressure side and suction side. This discontinuity occurred in various size of trailing edge circle and various angle of Psm and Ppm, which angle the trailing edge suction side and pressure side. It can be concluded that the fluctuation and spikes of pressure distribution along the designed Eppler will be minimised by accomplishing those issued mentioned. It will improve the capability of converged solution at higher angles of attack and provide better control for aerodynamic characteristics as well as blade desgin.

5 Appendices

5.1 Mathematical formulation for Weibull distribution of wind speed [7]

Wind energy characteristics for Weibull distribution and wind turbine characteristics	
Wind characteristics	
Mean wind speed	$V = c\Gamma\left(\frac{k+1}{k}\right)$
Standard deviation of wind speed	$\sigma = c\sqrt{\left[\Gamma\left(\frac{k+2}{k}\right) - \Gamma^2\left(\frac{k+1}{k}\right)\right]}$
Most probable wind speed	$V_{MP} = c\left(\frac{k-1}{k}\right)^{1/k}$
Wind speed carrying maximum energy	$V_{MaxE} = c\left(\frac{k+2}{k}\right)^{1/k}$
Mean wind power density	$\frac{P}{A} = \frac{1}{2}\rho c^3\Gamma\left(\frac{k+3}{k}\right)$
Mean wind energy density	$\frac{E}{A} = \frac{1}{2}\rho c^3\Gamma\left(\frac{k+3}{k}\right)T$
Wind turbine characteristics	
Wind energy generated by an ideal wind turbine	$E_{TW} = \frac{\rho}{2}TA\int_{V_I}^{V_R} V^n\frac{k}{c}\left(\frac{V}{c}\right)^{k-1} e^{-(V/c)^k}dV + \frac{\rho}{2}TAV_R^n\int_{V_R}^{V_O}\frac{k}{c}\left(\frac{V}{c}\right)^{k-1} e^{-(V/c)^k}dV$
Actual wind energy output from a wind turbine	$E_{TA} = TP_R\int_{V_I}^{V_R}(a_1V^n + a_2V^n + a_3V + a_4\frac{k}{c}\left(\frac{V}{c}\right)^{k-1} e^{-(V/c)^k}dV + TP_R\int_{V_R}^{V_O}\frac{k}{c}\left(\frac{V}{c}\right)^{k-1} e^{-(V/c)^k}dV$
Wind turbine efficiency	$\eta = \frac{E_{TA}}{E_{TW}}$
Rated wind energy	$E_{TR} = TP_R$
Capacity factor	$C_F = \frac{E_{TA}}{E_{TR}} = \int_{V_I}^{V_R}(a_1V^n + a_2V^n + a_3V + a_4\frac{k}{c}\left(\frac{V}{c}\right)^{k-1} e^{-(V/c)^k}dV + \int_{V_R}^{V_O}\frac{k}{c}\left(\frac{V}{c}\right)^{k-1} e^{-(V/c)^k}dV$
Availability factor	$A_F = P(V_I \le V < V_O) = \int_{V_I}^{V_O}\frac{k}{c}\left(\frac{V}{c}\right)^{k-1} e^{-(V/c)^k}dV$

The methods to determine a shape factor, k, and a scale factor, c are shown in [5].

5.2 Sample time series data for the average wind power density with density of 1.225 kg/m^3 [8]

Hour	Wind speed (m/s)			Hourly average wind speed (m/s)	Average wind power density (W/m^2)
	Day 1	Day 2	Day 3		
1	3.3	4.0	4.7	4.0	39.20
2	3.8	4.0	7.5	5.1	81.25
3	4.2	2.0	4.2	3.5	25.52
4	3.3	2.7	5.7	3.9	36.33
5	2.8	2.7	2.7	2.7	12.51
6	3.0	3.3	4.3	3.5	27.02
7	4.0	2.7	4.3	3.7	30.19
8	2.7	2.7	4.5	3.3	22.01
9	5.2	5.8	4.5	5.2	84.48
10	6.7	5.7	6.0	6.1	141.32
11	6.8	6.2	10.4	7.8	290.66
12	6.8	6.5	6.7	6.7	181.48
13	5.7	4.5	6.3	5.5	101.90
14	8.5	5.8	9.4	7.9	301.99
15	8.9	4.8	7.7	7.1	222.32
16	9.3	4.8	6.0	6.7	184.22
17	6.5	5.5	8.9	7.0	207.10
18	4.2	5.7	7.7	5.9	123.67
19	4.3	5.0	6.2	5.2	84.48
20	3.7	4.3	5.7	4.6	58.33
21	4.0	4.0	5.7	4.6	58.33
22	2.8	3.5	7.5	4.6	59.62
23	3.7	5.0	7.5	5.4	96.45
24	3.3	3.7	5.3	4.1	42.21

5.3 Size of specification of common industrial wind turbine [85]

Size specifications of common industrial wind turbines

Vestas and General Electric (GE) dominate the market for industrial wind turbines in the U.S. Many older U.S. facilities use NEG Micon turbines, and Vestas has absorbed that manufacturer. Other older facilities use turbines from Zond, which was acquired by Enron (the inventor of "green tags"), whose wind business GE acquired in turn to take over the racket. Information about Vestas models can be found at www.vestas.com, GE models at www.gepower.com/businesses/ge_wind_energy/en, Siemens Bonus models at www.powergeneration.siemens.com/en/windpower/products, Suzlon models at www.suzlon.com./product_overview.htm, Clipper models at www.clipperwind.com, REpower models at www.repower.de/index.php?id=12&L=1, Enercon, Fuhrländer, Mitsubishi, Nordex, and Ecotècnia are also major manufacturers, but their turbines do not appear to be currently used in the U.S.

model	capacity	blade length*	hub ht†	total ht	area swept by blades	rpm range	max blade tip speed‡	rated wind speed§
GE 1.5s	1.5 MW	35.25 m (116 ft)	64.7 m (212 ft)	99.95 m (328 ft)	3,904 m^2 (0.96 acre)	11.1-22.2	183 mph	12 m/s (27 mph)
GE 2.3	2.3 MW	47 m (154 ft)	100 m (328 ft)	147 m (482 ft)	6,940 m^2 (1.71 acres)	5.0-14.9	164 mph	~14 m/s (~31 mph)
GE 2.5	2.5 MW	44 m (144 ft)	85 m (279 ft)	129 m (423 ft)	6,082 m^2 (1.50 acres)	5.5-16.5	170 mph	~14.5 m/s (~32.5 mph)
GE 2.7	2.7 MW	42 m (138 ft)	70 m (230 ft)	112 m (336 ft)	5,542 m^2 (1.37 acres)	6.0-18.0	177 mph	~15 m/s (~34 mph)
Vestas V82	1.65 MW	41 m (135 ft)	70 m (230 ft)	111 m (364 ft)	5,281 m^2 (1.30 acres)	?-14.4	138 mph	13 m/s (29 mph)
Vestas V90	1.8 MW	45 m (148 ft)	80 m (262 ft)	125 m (410 ft)	6,362 m^2 (1.57 acres)	8.8-14.9	157 mph	11 m/s (25 mph)
Vestas V100	2.75 MW	50 m (164 ft)	80 m (262 ft)	130 m (427 ft)	7,854 m^2 (1.94 acres)	7.2-15.3	179 mph	15 m/s (34 mph)
			100 m (328 ft)	150 m (492 ft)				
Gamesa G87	2.0 MW	43.5 m (143 ft)	78 m (256 ft)	121.5 m (399 ft)	5,945 m^2 (1.47 acres)	9/19	194 mph	c. 13.5 m/s (30 mph)
Bonus (Siemens)	1.3 MW	31 m (102 ft)	68 m (223 ft)	99 m (325 ft)	3,019 m^2 (0.75 acres)	13/19	138 mph	14 m/s (31 mph)
Bonus (Siemens)	2.0 MW	38 m (125 ft)	60 m (197 ft)	98 m (322 ft)	4,536 m^2 (1.12 acres)	11/17	151 mph	c. 15 m/s (c. 34 mph)
Bonus (Siemens)	2.3 MW	41.2 m (135 ft)	80 m (262 ft)	121.2 m (398 ft)	5,333 m^2 (1.32 acres)	11/17	164 mph	c. 15 m/s (c. 34 mph)
Suzlon 950	0.95 MW	32 m (105 ft)	65 m (213 ft)	97 m (318 ft)	3,217 m^2 (0.79 acres)	13.9/20.8	156 mph	11 m/s (25 mph)
Suzlon S.64/1250	1.25 MW	32 m (105 ft)	73 m (240 ft)	105 m (344 ft)	3,217 m^2 (0.79 acres)	13.9/20.8	156 mph	12 m/s (27 mph)
Clipper Liberty	2.5 MW (4 × 650 KW)	44.5 m (146 ft)	80 m (262 ft)	124.5 m (409 ft)	6,221 m^2 (1.54 acres)	9.7-15.5	168 mph	c. 11.5 m/s (c. 26 mph)
		46.5 m (153 ft)		126.5 m (415 ft)	6,793 m^2 (1.68 acres)			c. 12.5 m/s (c. 28 mph)
		49.5 m (162 ft)		126.5 m (425 ft)	7,698 m^2 (1.90 acres)			c. 12.5 m/s (c. 28 mph)
REpower MM92	2.0 MW	46.25 m (152 ft)	100 m (328 ft)	146.25 m (480 ft)	6,720 m^2 (1.66 acres)	7.8-15.0	163 mph	11.2 m/s (25 mph)

*This figure is actually half the rotor diameter. The blade itself may be about a meter shorter, because it is attached to a large hub.
†Where different hub (tower) heights are available, the usually used size is presented.
‡Rotor diameter (m) × π × rpm ÷ 26.82
§The rated, or nominal, wind speed is the speed at which the turbine produces power at its full capacity. For example the GE 1.5s does not generate 1.5 MW of power until the wind is blowing steadily at 27 mph or more. As the wind falls below that, power production falls exponentially.

5.4 Vestas V90-3.0MW

the following date is from [19]

Example of Cp, Vestas V90-3.0MW

Density (kg/m^3)	1.225
Swept area (m^2)	6362

Wind speed (m/s)	Power available (kW)	power output (kW)	Cp
0	0	0	0
5	487	250	0.513
10	3,897	1750	0.449
15	13,151	3000	0.228
20	31,174	3000	0.096
25	60,886	3000	0.049

5.5 Eppler 387

5.5.1 The curvature calculations

x	y	ma	mb	X	Y	r	1/r (=C)	log r	log (1/r)	x
1	0	-0.1331	-0.1445	1.0742	0.56969	0.5745	1.74065	-0.2407	0.24071	1
0.99677	0.00043	-0.1445	-0.1587	1.1212	0.89492	0.90311	1.10729	-0.0443	0.04426	0.99677
0.98729	0.0018	-0.1587	-0.1643	1.51001	3.34462	3.38344	0.29556	0.52936	-0.52936	0.98729
0.97198	0.00423	-0.1643	-0.1636	-4.6931	-34.421	34.8885	0.02866	1.54268	-1.54268	0.97198
0.95128	0.00763	-0.1636	-0.1626	-4.0592	-30.546	30.9616	0.0323	1.49082	-1.49082	0.95128
0.92554	0.01184	-0.1626	-0.162	-8.1471	-55.684	56.4301	0.01772	1.75151	-1.75151	0.92554
0.8951	0.01679	-0.162	-0.162	-294.54	-1823.4	1847.16	0.00054	3.2665	-3.2665	0.8951
0.86035	0.02242	-0.162	-0.1614	-10.367	-69.162	70.0895	0.01427	1.84565	-1.84565	0.86035
0.82183	0.02866	-0.1614	-0.1597	-3.3602	-25.75	26.1153	0.03829	1.4169	-1.4169	0.82183
0.78007	0.0354	-0.1597	-0.1563	-1.4362	-13.701	13.9144	0.07187	1.14346	-1.14346	0.78007
0.73567	0.04249	-0.1563	-0.1506	-0.6223	-8.4938	8.64359	0.11569	0.93669	-0.93669	0.73567
0.68922	0.04975	-0.1506	-0.1427	-0.2662	-6.1297	6.25291	0.15993	0.79608	-0.79608	0.68922
0.64136	0.05696	-0.1427	-0.1292	0.09434	-3.603	3.70062	0.27022	0.56827	-0.56827	0.64136
0.59272	0.0639	-0.1292	-0.1086	0.25939	-2.325	2.41206	0.41458	0.38239	-0.38239	0.59272
0.54394	0.0702	-0.1086	-0.0816	0.32473	-1.7231	1.80668	0.5535	0.25688	-0.25688	0.54394
0.49549	0.07546	-0.0816	-0.0505	0.34666	-1.4543	1.537	0.65062	0.18667	-0.18667	0.49549
0.44767	0.07936	-0.0505	-0.0162	0.35605	-1.2685	1.35093	0.74023	0.13063	-0.13063	0.44767
0.40077	0.08173	-0.0162	0.02056	0.35809	-1.1426	1.22507	0.81628	0.08816	-0.08816	0.40077
0.35505	0.08247	0.02056	0.05815	0.35673	-1.0767	1.15917	0.86268	0.06415	-0.06415	0.35505
0.31078	0.08156	0.05815	0.0931	0.35929	-1.1206	1.20314	0.83116	0.08031	-0.08031	0.31078
0.26813	0.07908	0.0931	0.12826	0.35393	-1.0631	1.1454	0.87306	0.05896	-0.05896	0.26813
0.22742	0.07529	0.12826	0.1654	0.33904	-0.9469	1.02831	0.97247	0.01213	-0.01213	0.22742
0.18906	0.07037	0.1654	0.20701	0.31184	-0.7825	0.86168	1.16053	-0.0647	0.06466	0.18906
0.15345	0.06448	0.20701	0.25507	0.27764	-0.6173	0.69304	1.44292	-0.1592	0.15924	0.15345
0.12094	0.05775	0.25507	0.31275	0.23756	-0.4602	0.53091	1.88357	-0.275	0.27498	0.12094
0.09185	0.05033	0.31275	0.38605	0.19262	-0.3165	0.38041	2.62876	-0.4198	0.41975	0.09185
0.06643	0.04238	0.38605	0.48481	0.14768	-0.2001	0.25572	3.91058	-0.5922	0.59224	0.06643
0.04493	0.03408	0.48481	0.63094	0.10474	-0.1115	0.15739	6.3536	-0.803	0.80302	0.04493
0.02748	0.02562	0.63094	0.87942	0.06736	-0.0523	0.08751	11.427	-1.0579	1.05793	0.02748
0.01423	0.01726	0.87942	1.46737	0.0364	-0.0171	0.04086	24.4757	-1.3887	1.38874	0.01423
0.00519	0.00931	1.46737	-11.064	0.01045	0.00062	0.01015	98.4837	-1.9934	1.99336	0.00519
0.00044	0.00234	-11.064	-0.6326	0.00732	0.00034	0.00716	139.629	-2.145	2.14498	0.00044
0.00091	-0.0029	-0.6326	-0.2856	0.02234	0.02409	0.03443	29.0418	-1.463	1.46302	-0.0009
0.00717	-0.0068	-0.2856	-0.1454	0.04322	0.09718	0.11007	9.08478	-0.9583	0.95831	-0.0072
0.0189	-0.0102	-0.1454	-0.0717	0.06657	0.25784	0.27222	3.67348	-0.5651	0.56508	-0.0189
0.03596	-0.0127	-0.0717	-0.0274	0.08736	0.54775	0.56275	1.77699	-0.2497	0.24969	-0.036
0.05827	-0.0143	-0.0274	-0.0006	0.10254	1.10253	1.11766	0.89473	0.04831	-0.04831	-0.0583
0.08569	-0.015	-0.0006	0.01653	0.10309	2.00304	2.01811	0.49551	0.30495	-0.30495	-0.0857
0.118	-0.015	0.01653	0.02726	0.07631	3.62302	3.63828	0.27486	0.5609	-0.5609	-0.118
0.1549	-0.0144	0.02726	0.0339	-0.0011	6.46248	6.47877	0.15435	0.81149	-0.81149	-0.1549
0.19599	-0.0133	0.0339	0.03722	-0.2561	13.9865	14.007	0.07139	1.14635	-1.14635	-0.196
0.24083	-0.0118	0.03722	0.03822	-1.5827	49.6247	49.6699	0.02013	1.69609	-1.69609	-0.2408
0.28892	-0.01	0.03822	0.03766	3.86599	-92.939	92.9975	0.01075	1.96847	-1.96847	-0.2889
0.33968	-0.008	0.03766	0.03593	1.53389	-31.015	31.0301	0.03223	1.49178	-1.49178	-0.3397
0.39252	-0.0061	0.03593	0.03307	1.10737	-19.145	19.152	0.05221	1.28221	-1.28221	-0.3925
0.44679	-0.0041	0.03307	0.02957	0.99506	-15.749	15.7543	0.06347	1.1974	-1.1974	-0.4468
0.50182	-0.0023	0.02957	0.02549	0.92691	-13.444	13.4486	0.07436	1.12868	-1.12868	-0.5018
0.55694	-0.0007	0.02549	0.02103	0.89252	-12.095	12.0991	0.08265	1.08275	-1.08275	-0.5569
0.61147	0.00074	0.02103	0.01598	0.85595	-10.356	10.36	0.09652	1.01536	-1.01536	-0.6115
0.66472	0.00186	0.01598	0.01067	0.84085	-9.4121	9.41565	0.10621	0.97385	-0.97385	-0.6647
0.71602	0.00268	0.01067	0.00483	0.82653	-8.0695	8.07291	0.12387	0.90703	-0.90703	-0.716
0.76475	0.0032	0.00483	-0.0012	0.82248	-7.2322	7.23565	0.1382	0.85948	-0.85948	-0.7648
0.81027	0.00342	-0.0012	-0.008	0.82419	-5.8015	5.80493	0.17227	0.7638	-0.7638	-0.8103
0.85202	0.00337	-0.008	-0.015	0.83067	-4.9934	4.99679	0.20013	0.69869	-0.69869	-0.852
0.88944	0.00307	-0.015	-0.0227	0.84663	-3.9312	3.93448	0.25416	0.59489	-0.59489	-0.8894
0.92205	0.00258	-0.0227	-0.0294	0.85335	-3.6348	3.63799	0.27488	0.56086	-0.56086	-0.9221
0.94942	0.00196	-0.0294	-0.0384	0.89891	-2.0857	2.08823	0.47887	0.31978	-0.31978	-0.9494
0.97118	0.00132	-0.0384	-0.0516	0.94171	-0.9721	0.97388	1.02682	-0.0115	0.01149	-0.9712
0.98705	0.00071	-0.0516	-0.0644	0.96574	-0.5065	0.50765	1.96987	-0.2944	0.29444	-0.9871
0.99674	0.00021	-0.0644	0	0.5	-7.7365	7.75264	0.12899	0.88945	-0.88945	-0.9967
1	0	0	#DIV/0!	#DIV/0!	#DIV/0!	#DIV/0!	#DIV/0!	#DIV/0!	#DIV/0!	-1

5.5.2 Calculation of P_mech and C_x

The following table shows the calculation of mechanical power and the corresponding the wind speed and rotational speed by expanding the data from [82], which is very narrow information in the small range of wind speed. The relation between electrical power and mechanical power is as mentioned by Bak [82] that electrical power is 85% of mechanical power.

Eppler387, Calculation of P_{mech} and C_x

Cpmech	0.45
A (m2)	2.4053
ρ (kg/m3)	1.2
r (m)	0.875

$P_{electrical}$ (W)	P_{mech} (kW)	C_x (m/s)	rpm
25	0.0294	3.5645	
	0.0416	4	268.6
50	0.0588	4.4910	
	0.0592	4.5	
	0.0812	5	285.7
100	0.1176	5.6583	
	0.1403	6	302.8
	0.2228	7	366.2
200	0.2353	7.1290	
	0.3325	8	442.6
300	0.3529	8.1606	
400	0.4706	8.9819	
	0.4734	9	543.1
500	0.5882	9.6755	615
	0.6494	10	641.4
600	0.7059	10.2817	
700	0.8235	10.8239	
	0.8644	11	708.9
800	0.9412	11.3165	725

$P_{electrical}$ (W)	P_{mech} (kW)	C_x (m/s)	rpm
900	1.0588	11.7696	775
	1.1222	12	808.5
1000	1.1765	12.1903	820
	1.2684	12.5	
1100	1.2941	12.5839	
1200	1.4118	12.9542	
	1.4268	13	916.2
1300	1.5294	13.3045	
1400	1.6471	13.6372	
1500	1.7647	13.9545	
	1.7820	14	1023.9
1600	1.8824	14.2579	
1700	2.0000	14.5490	
1800	2.1176	14.8288	
	2.1918	15	
1900	2.2353	15.0985	
2000	2.3529	15.3589	
2100	2.4706	15.6107	
2200	2.5882	15.8547	

Figure 50 shows the slope of mechanical power generated at wind speeds, obtained from the table above. This graph determines the maximum power generation of the blade at the operating wind speeds.

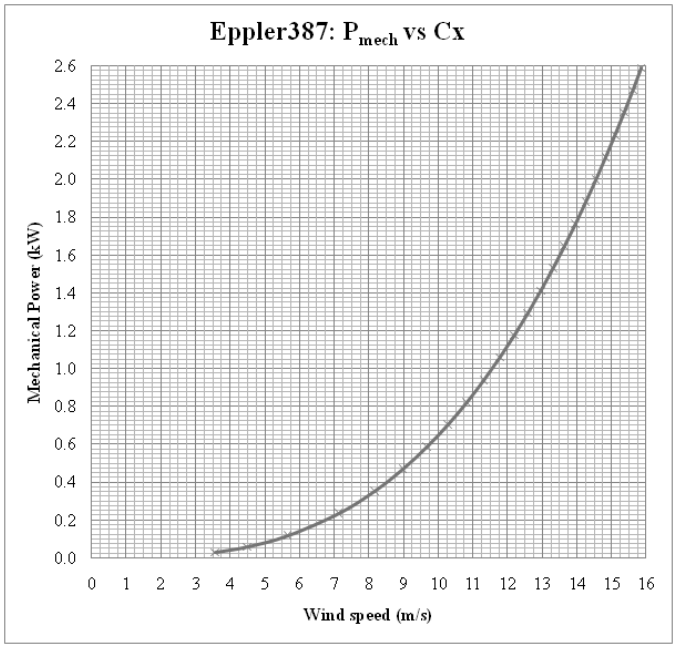

Figure 50: Mechanical power of Eppler387 generated at wind speeds

5.6 Designed Eppler387

5.6.1 Parameters of designed Eppler387 used in the programme of direct surface curvature distribution blade design method

alpha1	4
alpha2	2
LEposition	0
B	1
Lambda	-0.05
Xsm	0.5
Ysm	0.077
bsm	-5.12
bsr	-39.85
phiss	72
rte	0.001
k1s	1260
k2s	3200
k11s	-5030
k12s	-30
k13s	-2800
k14s	-50
xC1s	0.1
yC1s	1.3
xC2s	0.175
yC2s	1.29
yC3s	1.29
yC4s	1.1
xC5s	0.36
rle	0.00586
phip	-34
bpr	31.2
k1p	3890
k2p	3470
bpm	1.568
Xpm	0.3
Ypm	-0.008
xC1p	0.11
yC1p	0.034
xC2p	0.15

xC2p	0.15
yC2p	0.035
yC3p	0.035
yC4p	0.03
xC5p	0.24
k11p	-5030
k12p	-20
k13p	-2700
k14p	-10
rDSeita	0.01745
Xcns	0.16
Ycns	0.03
angle	10
Xcnp	0.14
Ycnp	0
angle1	0
xmin	-0.5
xmax	1
ymin	-0.5
ymax	1.5

References

[1] I. Ushiyama. Foundation of wind energy. *Ohmsha*, Japan. July 2005

[2] Department of Energy and Climate Change. Energy statics: total energy. Inland consumption of primary fuels and equivalents for energy use, 1970 to 2008. Available online http://www.decc.gov.uk, visited on September 2009 at, http://www.decc.gov.uk/en/content/cms/statistics/source/total/total.aspx

[3] S. L. Dixon. Fluid mechanics and thermodynamics of turbomachinery 5th edition. *Elsevier Butterworth-Heinemann*. UK. 2005

[4] Global Wind Energy Council (GWEC). Global wind 2008 report, Available online http://www.gwec.net, visited on April 2009 at, http://www.gwec.net/fileadmin/documents/Global

[5] J. F. Manwell, J. G. McGowan and A. L. Rogers. Wind Energy Explained, Theory, Design and Application. *John Wiley & Sons, LTD*. England. 2002

[6] C. L. Archer and M. Z. Jacobson Evaluation of global wind power. *Journal of geophysical research. vol.110, D12110, doi:10.1029/2004JD005462* March 2005

[7] T. J. Chang, Y. T. Wu, H. Y. Hsu, C. R. Chu and C. M. Liao. Assessment of wind characteristics and wind turbine characteristics in Taiwan. *Renewable energy. vol.28, no.6, pp.851-871.* May 2003

[8] J. V. Seguro, T. W. Lambert Modern estimation of the parameters of the Weibull wind speed distribution for wind energy analysis. *Journal of wind engineering and industrial aerodynamics. vol.85, no.1, pp.75-84.* March 2000

[9] A. C. Hansen, C. P. Butterfield. Aerodynamics of horizontal-axis wind turbines *Annu. Rev. Fluid Mech. 25:115-149*. 1993

[10] British Wind Energy Association. Energy Saving Trust Report: Small is Powerful,Even at current electricity prices 450,000 domestic locations ready for small wind. July 2009

[11] M. Lehnhoff and I. de Buhr Multibrid M5000, Assembly and installation of a 5MW wind turbine. November 2004

[12] Terra Magnetica. Why are wind turbines getting bigger?, Available on http://www.terramagnetica.com, visited on August 2009 at, http://www.terramagnetica.com/2009/08/01/why-are-wind-turbines-getting-bigger/

[13] C. Hochart, G. Fortin, J. Perron, A. Ilinca. Wind turbine performance under icing conditions. *Wind Energy. vol 11. issue 4. pp 319-333*. July-August 2008

[14] P. S. Veers, T. D. Ashwill, H. J. Sutherland, D. L. Laird, D. W. Lobitz, D. A. Griffin, J. F. Musial, K. Jackson, M. Zuteck, A. Miravete, S. W. Tsai and J. L. Richmond. Trends in the design, manufacture and evaluation of wind turbine blades. *Wind Energy. vol 6. pp 245-259*. 2003

[15] Wikipedia. Wind turbine, Available online, http://en.wikipedia.org, visited on October 2009 at, http://en.wikipedia.org/wiki/Windturbine

[16] Wikipedia. Wind turbine manufacturers, Available online, http://en.wikipedia.org, visited on October 2009 at, http://en.wikipedia.org/wiki/Windturbinemanufacturer

[17] Enercon. Windblatt, Energy for the world. ENERCON magazine for wind energy. Issue 03 2009. Aavailable online http://www.enercon.com/,

visited on October 2009 at, http://www.enercon.de/p/downloads/WB-0309-en.pdf

[18] J. Johansen, H. A. Madsen, M. Gaunaa and C. Bak. Design of a wind turbine rotor for maximum aerodynamic efficiency. *Wind energy, vol.21, no.3, pp.261-273*. 2009

[19] Vestas,V90-3.0MW. 3.0MW-An efficient way to more power. V90-3.0MW brochure

[20] J. L. Tangler. The evolution of rotor and blade design. *NREL, no.CP-500-28410*. July 2000

[21] S. H. Wang and S. H. Chen. Blade number effect for a ducted wind turbine. *Journal of mechanical science and technology 22(2008)1984-1992*. October 2008

[22] G. L. Johnson. Wind energy system, Electronic Edition. Manhattan, KS. December 2001

[23] Nordic Windpower. Arguments for large two-bladed wind turbines. Available online http://www.windpowerengineering.com, visited on September 2009 at, http://www.windpowerengineering.com/index.php?s=argument+for+large+two-bladed+wind+turbines

[24] M. C. Rector. Studying the effect of blade pitch on small multi-bladed horizontal-axis wind turbines. Honors thesis proposal

[25] P. Gipe. Wind power: Renewable energy for home, farm and business, completely revised and expanded edition. E-book. US. 2004

[26] D. G. Wilson and T. Korakianitis. The design of high-efficiency turbo-machinery and gas turbines, 2nd edition. Prentice Hall. January 1998

[27] G. Boyle. Renewable energy, Power for a sustainable future, 2nd edition. Oxford press. 2004

[28] E. A. Mayda, C. P. van Dam. Bubble-induced unsteadiness on a wind turbine airfoil. *Journal of solar energy engineering-transactions of the ASME. vol.124. issue.4. pp.335-344.* November 2002

[29] T. Korakianitis. A design method for the prediction of unsteady forces on subsonic, axial gas-turbine blades. Doctoral dissertation in mechanical engineering. Massachusetts Institute of technology. Cambridge. MA. USA. September 1987

[30] T. Korakianitis. Prescribed-curvature-distribution airfoils for the preliminary geometric design of axial-turbomachinery cascades. *Journal of turbomachinery. vol.115, no.2, pp.325-333.* April 1993

[31] O. P. Sharma, G. F. Pickett and R. H. Ni. Assessment of unsteady flow in turbines. *Journal of turbomachinery. vol.114.* January 1992

[32] I. A. Hamakhan and T. Korakianitis. Aerodynamic performance effects of leading edge geometry in gas turbine blades. *Applied energy.* June 2009

[33] M. S. Kamran. Airfoil optimization by prescribed surface curvature method. MSc dissertation. Queen Mary, University of London. August 2009

[34] T. Korakianitis and B. H. Wegge. Three dimensional direct turbine blade design method. *AIAA 2002-3347, 32nd fluid dynamics conference and exhibit.* St Louis. Missouri. June 2002

[35] M. Vlieghe. Airfoil design and modelisation. Internship report. . Queen Mary, University of London. September 2009

[36] K. S. Dahl and P. Fuglsang. Design of the wind turine airfoil family RISO-A-XX. *Riso-R-1024(EN). RISO National Laboratory*. Denmark. December 1998

[37] K. Ameku, B. M. Nagai and J. N. Roy. Design of a 3kW wind turbine generator with thin airfoil blades. *Experimental thermal and fluid science. vol.32, no.8, pp.1723-1730*. June 2008

[38] A. J. Vitale and A. P. Rossi. Computational method for the design of wind turbine blades. *International journal of hydrogen energy. vol.33, no.13, pp.3466-3470*. July 2008

[39] J. C. C. Henriques, F. Marques da Silva, A. I. Estanqueiro and L. M. C. Gato. Design of a new urban wind turbine airfoil using a pressure-load inverse method. *Renewable energy vol.34, no.12, pp.2728-2734* December 2009

[40] J. C. Pascoa, A. C. Mendes and L. M. C. Gato. A fast iterative inverse method for turbomachinery blade design. *Mechanics research communications. vol.36, no.5, pp.630-637*. July 2009

[41] L. de Vito, R. A. Van den Braembussche and H. Deconinck. A novel tow-dimensional viscous inverse design method for turbomachinery blading. *Journal of terbomachinery. vol.125, no.2, pp.310-316*. April 2003

[42] O. Leonard and R. A. Van den Braembussche. Design method for subsonic and transonic cascades with prescribed mach number distribution. *Journal of turbomachinery. vol.114, no.3, pp.553560*. July 1992

[43] A. Demeulenaere and R. A. Van den Braembussche. Three-dimensional inverse method for turbomachinery blading design. *Journal of turbomachinery. vol.120, no.1, pp.247255*. September 1996

[44] W. T. Tiow, K. F. C. Yiu and M. Zangeneh. Application of simulated annealing to inverse design of transonic turbomachinery cascades. *Journal of power and energy. vol.216, no.1, pp.59-73.* 2002

[45] L. Battisti and G. Soraperra and R. Fedrizzi and L. Zanne. Inverse design-momentum, a method for the preliminary design of horizontal axis wind turbines. *Journal of physics. vol.75, 012013.* 2007

[46] B. Kamoun and D. Afungchui and M. Abid. Inverse design of the wind turbine blade sections by the singularities method. *Renewable energy. vol.31, no.13 pp.2091-2107.* October 2006

[47] PROFOIL-WWW Version 1.1. Available online http://www.profoil.org, visited on September at, http://www.profoil.org/profoil/010-overview.html

[48] J. L. Tangler and D. M. Somers. NREL airfoil families for HAWTs. Windpower95 conference. Washington. 1995

[49] NACA airfoil series. Available online http://www.aerospaceweb.org, visited on October at, http://www.aerospaceweb.org/question/airfoils/q0041.shtml

[50] P. Fuglsang and C. Bak. Development of the Rios wind turbine airfoils. *Wind energy. vol.7, no.2, pp.145162.* May 2004

[51] H. Glaucrt. Windmills and fans.Aerodynamic Theory. *Springer. pp.434.* Berlin. 1935

[52] H. Glaucrt. Airscrew theory. Aerodynamic Theory. *Springer. pp.434.* Berlin. 1935

[53] R. E. Wilson and P. B. S. Lissaman. Applied aerodynamics of wind power machines. *GI-74113. Oregon State University. Corvallis. pp.118.* May1974

[54] Z. Ye, X. Liu and Y. Chen. Global optimum design method and software for the rotor blades of horizontal axis wind turbines. *Wind engineering. vol.26. no.4. pp.257-267.* 2002

[55] W. M. Foley. From daVinci to the present-a review of airscrew theory for helicopters, propellers, windmills and engines. *AlAA. vol.12, pp.76-367.* New York. 1976

[56] W. van Gent. Unsteady lifting-surface theory for ship screws; derivation and numerical treatment of integral equation. *Journal of ship research. vol.19, pp.243-253.* 1975

[57] E. Suciu, R. Preuss, L. Morino. Potential aerodynamic analysis of horizontal-axis windmills. *AIAA. vol.10, pp.77-132.* New York. 1977

[58] R. D. Preuss, E. O. Sueiu and L. Morino. Unsteady potential aerodynamics of rotors with applications to horizontal-axis windmills. *A1AA. vol.18, no.4, pp.385-393.* 1980

[59] L. A. Viterna and R. D. Corrigan. Fixed pitch rotor performance of large HAWTs. DOE/NASA Workshop on Large HAWTs. Cleveland, OH. 1981

[60] K. L. Jackson and P. G. Migliore. Design of wind turbine blades employing advanced airfoils. Windpower conference'87. San Francisco. CA. 1987

[61] C. Thumthae and T. Chitsomboon. Optimal angle of attack for untwisted blade wind turbine. *Renewable energy. vol.34, no.5, pp.1279-1284.* May 2009

[62] D. C. Hill and A. D. Garrad. Design of airfoils for wind turbine use. European wind energy conference. Glasgow. Scotland. 1989

[63] C. A. Morgan and A. D. Garrad. The design of optimum rotors for HAWTs. British wind energy association. Wind energy conference. London. 1988

[64] M. C. Robinson, M. M. Hand, D. A. Simms and S. J. Schreck. Horizontal axis wind turbine aerodynamics: three-dimensional, unsteady, and separated flow influences. *NREL/CP-500-26337*. July 1999

[65] J. L. Tangler. Insight into wind turbine stall and post-stall aerodynamics. *Wind energy. vol.7, no.3, pp.247-260* 2004.

[66] S. Schreck and M. Robinson. Rotational augmentation of horizontal axis wind turbine blades aerodynamic response. *Wind energy. vol.5, no.2-3, pp.133-150*. July 2002

[67] S. J. Schreck and M. Robinson Horizontal axis wind turbine blade aerodynamics in experiments and modeling. *Transactions on energy conversion. vol.22, no.1, pp.61-70*. March 2007

[68] A. Filippone. Airfoil inverse design and optimization by means of viscous and inviscid techniques. *Wind engineering and industrial aerodynamics. vol.56, no.2-3, pp.123-136*. 1993

[69] X. Liu, Y. Chen and Z. Ye. Optimization model for rotor blades of horizontal axis wind turbines. *Frontiers of mechanical engineering in China. vol.2, no.4, pp.483-488*. September 2007

[70] K. Y. Maalawi and M. T. S. Badawy. A direct method for evaluating performance of Horizontal axis wind turbines. *Renewable and sustainable energy reviews. vol.5, no.2, pp.175-190*. June 2001

[71] J. J. Chattot. Optimization of wind turbines using helicoidal vortex model. *Solar energy engineering. vol.125, no.4, pp.418-424*. November 2003

[72] A. Maheri, S. Noroozi and J. Vinney. Decoupled aerodynamic and structural design of wind turbine adaptive blades. *Renewable energy. vol.32, no.10, pp.1753-1767.* August 2007

[73] S. M. Habali and I. A. Saleh. Design and testing of small mixed airfoil wind turbine blades. *Renewable energy. vol.6, no.2, pp.161-169.* 1995

[74] C. Sicot, S. Aubruna, S. Loyer and P. Devinant. Unsteady characteristics of the static stall of an airfoil subjected to freestream turbulence level up to 16%. *Experiments in fluids. vol.41, no.4, pp.641-648.* October 2006

[75] C. Sicot, P. Devinant, T. Laverne, S. Loyer and J. Hureau. Experimental study of the effect of turbulence on horizontal axis wind turbine aerodynamics. *Wind energy. vol.9, no.4, pp.361-370.* 2006

[76] C. Sicot, P. Devinant, S. Loyer and J. Hureau. Rotational and turbulence effects on a wind turbine blade. Investigation of the stall mechanism. *Journal of wind engineering and industrial aerodynamics. vol.96, no.8-9, pp.1320-1331.* 2008

[77] D. M. Somers and M. D. Maughmer. Theoretical aerodynamic analyses of sic airfoil for use on small wind turbines. *National renewable energy laboratory (NREL). SR-500-33295. US.* June 2003

[78] F. Bertagnolio, N. Sorensen, J. Johansen and P. Fuglsang. Wind turbine airfoil catalogue. Riso-R-1280. *Riso National Laboratry. Roskilde, Denmark.* August 2001

[79] Moody diagram. Available online http://www.engineeringtoolbox.com, visited on October 2009 at, http://www.engineeringtoolbox.com/moody-diagram-d618.html

[80] S. M. Salim and S. C. Cheah. Wall y+ strategy for dealing with wall-bounded turbulent flows. The international multiconference of engineers and computer scientists 2009. vol 2, IMECS 2009. Hong Kong. March 2009

[81] Equation of a circle from 3 points in 2D. Available online http://local.wasp.uwa.edu.au, visited on November 2009 at, http://local.wasp.uwa.edu.au/ pbourke/geometry/circlefrom3/

[82] C. Bak and P. Fuglsang. Design of a 1.75-meter rotor for the Windsave wind turbine. *Riso National Laboratry. Roskilde, Denmark*. April 2004

[83] K. Rahman. Energy, entropy and exergy balances in a renewable energy laboratory: Wind turbine CFD analysis. 4th year group project. Queen Mary, University of London. 2008

[84] D. M. Somers. The S814 and S815 airfoils. *National renewable energy laboratory (NREL). SR-500-36292. US*. December 2004

[85] AWEO. Size of specification of common industrial wind turbine. Available online http://docs.wind-watch.org, visited on November 2009 at, http://docs.wind-watch.org/windturbinespecs.pdf